

Training-free linear image inverses via flows

Anonymous authors

Paper under double-blind review

Abstract

Solving inverse problems without any training involves using a pretrained generative model and making appropriate modifications to the generation process to avoid finetuning of the generative model. While recent methods have explored the use of diffusion models, they still require the manual tuning of many hyperparameters for different inverse problems. In this work, we propose a training-free method for solving linear inverse problems by using pretrained flow models, leveraging the simplicity and efficiency of Flow Matching models, using theoretically-justified weighting schemes, and thereby significantly reducing the amount of manual tuning. In particular, we draw inspiration from two main sources: adopting prior gradient correction methods to the flow regime, and a solver scheme based on conditional Optimal Transport paths. As pretrained diffusion models are widely accessible, we also show how to practically adapt diffusion models for our method. Empirically, our approach requires no problem-specific tuning across an extensive suite of noisy linear inverse problems on high-dimensional datasets, ImageNet-64/128 and AFHQ-256, and we observe that our flow-based method for solving inverse problems improves upon closely-related diffusion-based methods in most settings.



Figure 1: Corrected images by solving linear inverse problems with flow models. For each pair of images, we show the noisy measurement (left) and the reconstruction (right).

1 Introduction

Solving an inverse problem involves recovering a clean signal from noisy measurements generated by a known degradation model. Many interesting image processing tasks can be cast as an inverse problem. Some instances of these problems are super-resolution, inpainting, deblurring, colorization, denoising etc. Diffusion models or score-based generative models (Sohl-Dickstein et al., 2015; Ho et al., 2020; Song & Ermon, 2019; Song et al., 2021c) have emerged as a leading family of generative models for solving inverse problems for images (Saharia et al., 2022b;a; Wang et al., 2022; Chung et al., 2022a; Song et al., 2022; Mardani et al., 2023). However, sampling with diffusion models is known to be slow, and the quality of generated images is affected by the curvature of SDE/ODE solution trajectories (Karras et al., 2022). While Karras et al. (2022) observed ODE sampling for image generation could produce better results, sampling via SDE is still common for solving inverse problems, whereas ODE sampling has been rarely considered, perhaps due to the use of diffusion probability paths.

Continuous Normalizing Flow (CNF) (Chen et al., 2018b) trained with Flow Matching (Lipman et al., 2022) has been recently proposed as a powerful alternative to diffusion models. CNF (hereafter denoted flow model) has the ability to model arbitrary probability paths, and includes diffusion probability paths as a special case. Of particular interest to us are Gaussian probability paths that correspond to optimal transport (OT) displacement (McCann, 1997). Recent works (Lipman et al., 2022; Albergo & Vanden-Eijnden, 2022; Liu et al., 2022; Shaul et al., 2023) have shown that these conditional OT probability paths are straighter than diffusion paths, which results in faster training and sampling with these models. Due to these properties, conditional OT flow models are an appealing alternative to diffusion models for solving inverse problems.

In this work, we introduce a training-free method to utilize pretrained flow models for solving linear inverse problems. Our approach adds a correction term to the vector field that takes into account knowledge from the degradation model. Specifically, we introduce an algorithm that incorporates IIGDM (Song et al., 2022) gradient correction to flow models. Given the wide availability of pretrained diffusion models, we also present a way to convert these models to arbitrary paths for our sampling procedure. Empirically, we observe images restored via a conditional OT path exhibit perceptual quality better than that achieved by the model’s original diffusion path, as well as recently proposed diffusion approaches such as IIGDM (Song et al., 2022) and RED-Diff (Mardani et al., 2023), particularly in noisy settings. To summarize, our key contributions are:

- We present a training-free approach for solving linear inverse problems with pretrained conditional OT flow models that adapts the IIGDM correction, proposed for diffusion models, to flow sampling.
- We offer a way to convert between flow models and diffusion models, enabling the use of pretrained continuous-time diffusion models for conditional OT sampling, and vice versa.
- We demonstrate that images restored via our algorithm using conditional OT probability paths have perceptual quality that is largely on par with, or better than that achieved by diffusion probability paths, and other recent methods like IIGDM and RED-Diff, without the need for problem-specific hyperparameter tuning.

2 Preliminaries

We introduce relevant background knowledge and notation from conditional diffusion and flow modeling, as well as training-free inference with diffusion models.

Notation. Both diffusion and flow models consider two distinct processes indexed by time between $[0, 1]$ that convert data to noise and noise to data. Here, we follow the temporal notation used in prior work (Lipman et al., 2022) where the distribution at $t = 1$ is the data distribution and $t = 0$ is a standard Gaussian distribution. Note that this is opposite of the prevalent notation used in diffusion model literature (Song & Ermon, 2019; Ho et al., 2020; Song et al., 2021a;c). We let \mathbf{x}_t denote the value at time t , without regard to which process (*i.e.*, diffusion or flow) it was drawn from. The probability density for the data to noise process is denoted q and the parameterized probability density for the noise to data process is denoted p_θ . Expectations with respect to q are denoted via \mathbb{E}_q . We generally keep function arguments of t implicit (*i.e.* $f(\mathbf{x}_t, t)$ is informally written as $f(\mathbf{x}_t)$.)

Conditional diffusion models. Conditional diffusion uses a class of processes q , and defines data to noise process p_θ as a Markov process that in continuous time obeys a stochastic differential equation (SDE) (Song & Ermon, 2019; Ho et al., 2020; Song et al., 2021c). The parameters of p_θ are learned via minimizing a regression loss with respect to \widehat{x}_1

$$L_{\text{diffusion}}(\widehat{x}_1, q) = \int_0^1 w(t) \mathbb{E}_q[(\widehat{x}_1(x_t, \mathbf{y}) - x_1)^2] dt \quad (1)$$

where $w(t)$ are positive weights (Kingma et al., 2021; Song et al., 2021b; Kingma & Gao, 2023), \mathbf{y} is conditioning (i.e. a noisy image), and x_1 is noiseless data. The optimal solution for \widehat{x}_1 is $\mathbb{E}_q[x_1|x_t, \mathbf{y}]$, and hence we refer to \widehat{x}_1 as a denoiser. Many equivalent parameterizations exist and have known conversions to denoising. Sampling using p_θ proceeds via starting from $x_0 \sim p_\theta(x_0|\mathbf{y})$ and integrating the SDE to $t = 1$. If $p_\theta(x_0|\mathbf{y}) = q(x_0|\mathbf{y})$, the SDE is integrated exactly, and $\widehat{x}_1 = \mathbb{E}_q[x_1|x_t, \mathbf{y}]$, the resulting $x_1 \sim q(x_1|\mathbf{y})$.

Conditional flow models Alternatively, continuous normalizing flow models (Chen et al., 2018b) define the data generation process through an ODE. This leads to simpler formulations and does not introduce extra noise during intermediate steps of sample generation. Recently, simulation-free training algorithms have been designed specifically for such models (Lipman et al., 2022; Liu et al., 2022; Albergo & Vanden-Eijnden, 2022), an example being the Conditional Flow Matching loss (Lipman et al., 2022),

$$L_{\text{cfm}}(\widehat{\mathbf{v}}, q) = \int_0^1 \mathbb{E}_q \left[\left(\widehat{\mathbf{v}}(x_t, \mathbf{y}) - \mathbb{E}_q \left[\frac{d\mathbf{x}_t}{dt} \middle| x_t, \mathbf{y}, x_1 \right] \right)^2 \right] dt. \quad (2)$$

where $\widehat{\mathbf{v}}(x_t, \mathbf{y})$ denotes a parameterized vector field defining the ODE

$$\frac{d\mathbf{x}_t}{dt} = \widehat{\mathbf{v}}(x_t, \mathbf{y}). \quad (3)$$

If trained perfectly, the marginal distributions of x_t , denoted $p_\theta(x_t|\mathbf{y})$, will match the marginal distributions of $q(x_t|\mathbf{y})$. Hence sampling from $q(x_t|\mathbf{y})$ involves starting from an initial value $x_{t'} \sim q(x_{t'}|\mathbf{y})$ and integrating the ODE from t' to t . Typically, one samples from $t' = 0$ since $q(x_0|\mathbf{y})$ is a tractable distribution. For general Gaussian probability paths $q(x_t|x_1, \mathbf{y}) = \mathcal{N}(\mu_t(\mathbf{y}, x_1), \sigma_t(\mathbf{y}, x_1)^2 \mathbf{I})$, one can set (Lipman et al., 2022)

$$\mathbb{E}_q \left[\frac{d\mathbf{x}_t}{dt} \middle| x_t, \mathbf{y}, x_1 \right] = \frac{d\mu_t}{dt} + \frac{d\sigma_t}{dt} \left(\frac{x_t - \mu_t}{\sigma_t} \right). \quad (4)$$

Gaussian probability paths. The time-dependent distributions $q(x_t|\mathbf{y}, x_1)$ are referred to as conditional probability paths. We focus on the class of affine Gaussian probability paths of the form

$$q(x_t|\mathbf{y}, x_1) = q(x_t|x_1) = \mathcal{N}(\alpha_t x_1, \sigma_t^2 \mathbf{I}) \quad (5)$$

where non-negative α_t and σ_t are monotonically increasing and decreasing respectively. This class includes the probability paths for conditional diffusion as well as the conditional Optimal Transport (OT) path (Lipman et al., 2022), where $\alpha_t = t$ and $\sigma_t = 1 - t$. The conditional OT path used by flow models has been demonstrated to have good empirical properties, including faster inference and better sampling in practice, and has theoretical support in high-dimensions (Shaul et al., 2023). As emphasized in Lin et al. (2023), a desirable property for probability paths, obeyed by conditional OT but not commonly used diffusion paths, is to ensure $q(x_0|\mathbf{y})$ is known (i.e. $\mathcal{N}(0, \mathbf{I})$), as otherwise one cannot exactly sample x_0 which can add substantial error.

Training-free conditional inference using unconditional diffusion. Given pretrained *unconditional* diffusion models that are trained to approximate $\mathbb{E}_q[x_1|x_t]$, training-free approaches aim to approximate $\mathbb{E}_q[x_1|x_t, \mathbf{y}]$. Under Gaussian probability paths, the two terms are related as Tweedie’s identity (Robbins, 1992) expresses $\mathbb{E}_q[x_1|x_t, \mathbf{y}] = (x_t + \sigma_t^2 \nabla_{x_t} \ln q(x_t|\mathbf{y}))/\alpha_t$. Applying this identity (twice for both $\mathbb{E}_q[x_1|x_t, \mathbf{y}]$ and $\mathbb{E}_q[x_1|x_t]$) and simplifying gives

$$\mathbb{E}_q[x_1|x_t, \mathbf{y}] = \mathbb{E}_q[x_1|x_t] + \frac{\sigma_t^2}{\alpha_t} \nabla_{x_t} \ln q(\mathbf{y}|x_t). \quad (6)$$

Following Eq. 6, past approaches (e.g., Chung et al. (2022a); Song et al. (2022)) have used the pretrained model for the first term and approximated the second intractable term to produce an approximate $\widehat{\mathbf{x}}_1(\mathbf{x}_t, \mathbf{y})$. Diffusion posterior sampling (DPS) (Chung et al., 2022a) proposed to approximate $q(\mathbf{y}|\mathbf{x}_t)$ via $q(\mathbf{y}|\mathbf{x}_1 = \widehat{\mathbf{x}}_1(\mathbf{x}_t))$. Later, Pseudo-inverse Guided Diffusion Models (PIGDM) (Song et al., 2022) improved upon DPS for linear noisy observations where $\mathbf{y} = \mathbf{A}\mathbf{x} + \sigma_y\epsilon$, where \mathbf{A} is some measurement matrix and $\epsilon \sim \mathcal{N}(0, \mathbf{I})$, by approximating $q(\mathbf{y}|\mathbf{x}_t)$ as $\mathcal{N}(\mathbf{A}\widehat{\mathbf{x}}_1(\mathbf{x}_t), \sigma_y^2\mathbf{I} + r_t^2\mathbf{A}\mathbf{A}^T)$, derived via first approximating $q(\mathbf{x}_1|\mathbf{x}_t)$ as $\mathcal{N}(\widehat{\mathbf{x}}_1(\mathbf{x}_t), r_t^2\mathbf{I})$. PIGDM also suggested adaptive weighting, replacing σ_t^2/α_t with another function of time to account for the approximation.

3 Solving Linear Inverse Problems without Training via Flows

In the standard setup of a linear inverse problem, we observe measurements $\mathbf{y} \in \mathbb{R}^n$ such that

$$\mathbf{y} = \mathbf{A}\mathbf{x}_1 + \epsilon \quad (7)$$

where $\mathbf{x}_1 \in \mathbb{R}^m$ is drawn from an unknown data distribution $q(\mathbf{x}_1)$, $\mathbf{A} \in \mathbb{R}^{n \times m}$ is a known measurement matrix, and $\epsilon \sim \mathcal{N}(0, \sigma_y^2\mathbf{I})$ is unknown *i.i.d.* Gaussian noise with known standard deviation σ_y . Given a pretrained flow model with $\widehat{\mathbf{v}}(\mathbf{x}_t)$ that can sample from $q(\mathbf{x}_1)$, and measurements \mathbf{y} , our goal is to produce clean samples from the posterior $q(\mathbf{x}_1|\mathbf{y}) \propto q(\mathbf{y}|\mathbf{x}_1)q(\mathbf{x}_1)$ without training a problem-specific conditional flow model defined by $\widehat{\mathbf{v}}(\mathbf{x}_t, \mathbf{y})$. Proofs are in Appendix A.

3.1 Converting between diffusion models and flow models

While our proposed algorithm is based on flow models, this poses no limitation on needing pretrained flow models. We first take a brief detour outside of inverse problems to demonstrate continuous-time diffusion models parameterized by $\widehat{\mathbf{x}}_1$ can be converted to flow models $\widehat{\mathbf{v}}$ that have Gaussian probability paths described by Eq. 5. We separate training and sampling such that one can train with Gaussian probability path q' and then perform sampling with a different Gaussian probability path q . Equivalent expressions to this subsection have been derived in Karras et al. (2022), leveraging a more general conversion from SDE to probability flow ODE from Song et al. (2021c). Karras et al. (2022) similarly separate training and sampling for Gaussian probability paths, and demonstrate that using alternative sampling paths was beneficial. Our derivations avoid the SDE via a flow perspective and exposes a subtlety when swapping probability paths using pretrained models.

Lemma 1. *For Gaussian probability path q given by Eq. 5, the optimal solution for $\widehat{\mathbf{v}}(\mathbf{x}_t, \mathbf{y})$ is known given $\mathbb{E}_q[\mathbf{x}_1|\mathbf{x}_t, \mathbf{y}]$, and vice versa.*

In particular, a diffusion model’s denoiser $\widehat{\mathbf{x}}_1(\mathbf{x}_t, \mathbf{y})$ trained using Gaussian probability path q can be interchanged with a flow model’s $\widehat{\mathbf{v}}(\mathbf{x}_t, \mathbf{y})$ with the same q via

$$\widehat{\mathbf{v}} = \left(\alpha_t \frac{d \ln(\alpha_t/\sigma_t)}{dt} \right) \widehat{\mathbf{x}}_1 + \frac{d \ln \sigma_t}{dt} \mathbf{x}_t. \quad (8)$$

Furthermore, $\widehat{\mathbf{x}}_1(\mathbf{x}_t, \mathbf{y})$ trained under q' can be used for another Gaussian q during sampling.

Lemma 2. *Consider two Gaussian probability paths q and q' defined by Eq. 5 with α_t, σ_t and α'_t, σ'_t respectively. Define $t'(t)$ as the unique solution to $\frac{\sigma_t}{\alpha_t} = \frac{\sigma'_{t'}}{\alpha'_{t'}}$ when it exists for given t . Then*

$$\mathbb{E}_q[\mathbf{x}_1|\mathbf{x}_t, \mathbf{y}] = \mathbb{E}_{q'}[\mathbf{x}_1|\mathbf{x}'_{t'} = \alpha'_{t'}\mathbf{x}_t/\alpha_t, \mathbf{y}]. \quad (9)$$

So if $\widehat{\mathbf{x}}_1$ was trained under q' it can be used for sampling under q via evaluating at $\widehat{\mathbf{x}}_1(\alpha'_{t'}\mathbf{x}_t/\alpha_t, t'(t), \mathbf{y})$ (with explicit time for clarity) whenever $t'(t)$ exists. In particular, if pre-trained denoiser was trained with q' and we perform conditional OT sampling, we utilize

$$t'(t) = \text{SNR}_{q'}^{-1}(\text{SNR}_q(t)) = \text{SNR}_{q'}^{-1} \left(\frac{t}{1-t} \right). \quad (10)$$

where signal-to-noise ratio $\text{SNR}(t) = \alpha_t/\sigma_t$. The main avenue for non-existence for $t'(t)$ is if the model under q' is trained using a minimum SNR above zero, which induces a minimum t for which $t'(t)$ exists. When a minimum t exists,

we can only perform sampling with q starting from $\mathbf{x}_t \sim q(\mathbf{x}_t|\mathbf{y})$. Approximating this sample is entirely analogous to approximating $\mathbf{x}_0 \sim q'(\mathbf{x}_0|\mathbf{y})$. This error already exists for q' because $q'(\mathbf{x}_0|\mathbf{y})$ is not $\mathcal{N}(0, \mathbf{I})$ unless q' is trained to zero SNR. An initialization problem cannot be avoided if q' has limited SNR range by switching paths to q .

3.2 Correcting the vector field of flow models

To solve linear inverse problems without any training via flow models, we derive an expression similar to Eq. 6 that relates conditional vector fields under Gaussian probability paths to unconditional vector fields.

Theorem 1. *Let q be a Gaussian probability path described by Eq. 5. Assume we observe $\mathbf{y} \sim q(\mathbf{y}|\mathbf{x}_1)$ for arbitrary $q(\mathbf{y}|\mathbf{x}_1)$ and $v(\mathbf{x}_t)$ is a vector field enabling sampling $\mathbf{x}_t \sim q(\mathbf{x}_t)$. Then a vector field $v(\mathbf{x}_t, \mathbf{y})$ enabling sampling $\mathbf{x}_t \sim q(\mathbf{x}_t|\mathbf{y})$ can be written*

$$v(\mathbf{x}_t, \mathbf{y}) = v(\mathbf{x}_t) + \sigma_t^2 \frac{d \ln(\alpha_t / \sigma_t)}{dt} \nabla_{\mathbf{x}_t} \ln q(\mathbf{y}|\mathbf{x}_t). \quad (11)$$

We turn Theorem 1 into an training-free algorithm for solving linear inverse using flows by adapting IIGDM’s approximation. In particular, given $\hat{v}(\mathbf{x}_t)$ (or $\hat{\mathbf{x}}_1(\mathbf{x}_t)$), our approximation will be

$$\hat{v}(\mathbf{x}_t, \mathbf{y}) = \hat{v}(\mathbf{x}_t) + \sigma_t^2 \frac{d \ln(\alpha_t / \sigma_t)}{dt} \gamma_t \nabla_{\mathbf{x}_t} \ln q^{app}(\mathbf{y}|\mathbf{x}_t), \quad (12)$$

where following IIGDM terminology, we refer to $\gamma_t = 1$ as unadaptive and other choices as adaptive weights. In general, we view adaptive weights $\gamma_t \neq 1$ as an adjustment for error in $q^{app}(\mathbf{y}|\mathbf{x}_t)$.

For $q^{app}(\mathbf{y}|\mathbf{x}_t)$, we generalize IIGDM to any Gaussian probability path described by Eq. 5 via updating r_t^2 . We still have $q^{app}(\mathbf{y}|\mathbf{x}_t)$ is $\mathcal{N}(\mathbf{A}\hat{\mathbf{x}}_1(\mathbf{x}_t), \sigma_y^2 \mathbf{I} + r_t^2 \mathbf{A}\mathbf{A}^\top)$ when $q(\mathbf{x}_1|\mathbf{x}_t)$ is approximated as $\mathcal{N}(\hat{\mathbf{x}}_1(\mathbf{x}_t), r_t^2 \mathbf{I})$. We choose r_t^2 by following IIGDM’s derivation, noting that if $q(\mathbf{x}_1)$ is $\mathcal{N}(0, \mathbf{I})$ and $q(\mathbf{x}_t|\mathbf{x}_1)$ is $\mathcal{N}(\alpha_t \mathbf{x}_1, \sigma_t^2 \mathbf{I})$, then

$$r_t^2 = \frac{\sigma_t^2}{\sigma_t^2 + \alpha_t^2}. \quad (13)$$

When $\alpha_t = 1$, we recover IIGDM’s r_t^2 as expected under their Variance-Exploding path specification.

Starting flow sampling at time $t > 0$. Initializing conditional diffusion model sampling at $t > 0$ has been proposed by Chung et al. (2022c). For flows, we similarly want $\mathbf{x}_t \sim q(\mathbf{x}_t|\mathbf{y})$ at initialization time t . In our experiments, we examine (approximately) initializing at different times $t > 0$ using

$$\mathbf{x}_t = \alpha_t \mathbf{y} + \sigma_t \epsilon \quad (14)$$

for $\epsilon \sim \mathcal{N}(0, \mathbf{I})$ when \mathbf{y} is the correct shape. For super-resolution, we use nearest-neighbor interpolation on \mathbf{y} instead. We also consider using $\mathbf{A}^\dagger \mathbf{y}$ as an ablation in the Appendix C (where \mathbf{A}^\dagger is the pseudo-inverse of \mathbf{A} (Song et al., 2022)). We may be forced to use this initialization for flow sampling due to converting a diffusion model not trained to zero SNR. However as shown in (Chung et al., 2022c) for diffusion, this initialization can improve results more generally. Conceptually, if the resulting \mathbf{x}_t is closer to $\mathbf{x}_t \sim q(\mathbf{x}_t|\mathbf{y})$ than achieved via starting from an earlier time t' and integrating, then this initialization can result in less overall error.

Algorithm summary. Putting this altogether, our proposed approach using flow sampling and conditional OT probability paths is succinctly summarized in Algorithm 1, derived via inserting $\alpha_t = t$ and $\sigma_t = 1 - t$. Unlike IIGDM, we propose unadaptive weights $\gamma_t = 1$. By default, we set initialization time $t = 0.2$. The algorithm therefore has no additional hyperparameters to tune over traditional diffusion or flow sampling. In Appendix B, we detail our algorithm for other Gaussian probability paths, and the equivalent formulation when a pretrained vector field is available instead.

4 Experiments

Datasets. We verify the effectiveness of our proposed approach on three datasets: face-blurred ImageNet 64×64 and 128×128 (Deng et al., 2009; Russakovsky et al., 2015; Yang et al., 2022), and AnimalFacesHQ (AFHQ) 256×256 (Choi et al., 2020). We report our results on 10K randomly sampled images from validation split of ImageNet, and 1500 images from test split of AFHQ.

Algorithm 1 Solving linear inverse problems via flows using conditional OT probability path

Require: Pretrained denoiser $\widehat{x}_1(x_t)$ converted to conditional OT probability path using Section 3.1, noisy measurement y , measurement matrix A , initial time t , and std σ_y

- 1: Initialize $x_t = ty + (1 - t)\epsilon$, where $\epsilon \sim \mathcal{N}(0, I)$ ▷ Initialize x_t , Eq. (14)
- 2: $z_t = x_t$
- 3: **for** each time step t' of ODE integration **do** ▷ Integrate ODE from $t' = t$ to 1.
- 4: $r_{t'}^2 = \frac{(1-t')^2}{t'^2 + (1-t')^2}$ ▷ Value of r_t^2 from Eq. (13)
- 5: $\widehat{v} = \frac{\widehat{x}_1(z_{t'}) - z_{t'}}{1-t'}$ ▷ Convert \widehat{x}_1 to vector field, Eq. (8)
- 6: $g = (y - A\widehat{x}_1)^\top (r_{t'}^2 AA^\top + \sigma_y^2 I)^{-1} A \frac{\partial \widehat{x}_1}{\partial z_{t'}}$ ▷ IIGDM correction
- 7: $\widehat{v}_{\text{corrected}} = \widehat{v} + \frac{1-t'}{t'} g$ ▷ Correct unconditional vector field \widehat{v} , Eq. (12)
- 8: **end for**

Tasks. We report results on the following linear inverse problems: inpainting (center-crop), Gaussian deblurring, super-resolution, and denoising. The exact details of the measurement operators are: 1) For inpainting, we use centered mask of size 20×20 for ImageNet-64, 40×40 for ImageNet-128, and 80×80 for AFHQ. In addition, for images of size 256×256 , we also use free-form masks simulating brush strokes similar to the ones used in Saharia et al. (2022a); Song et al. (2022). 2) For super-resolution, we apply bicubic interpolation to downsample images by $4 \times$ for datasets that have images with resolution 256×256 and downsample images by $2 \times$ otherwise. 3) For Gaussian deblurring, we apply Gaussian blur kernel of size 61×61 with intensity value 1 for ImageNet-64 and ImageNet-128, and 61×61 with intensity value 3 for AFHQ. 4) For denoising, we add *i.i.d.* Gaussian noise with $\sigma_y = 0.05$ to the images. For tasks besides denoising, we consider *i.i.d.* Gaussian noise with $\sigma_y = 0$ and 0.05 to the images. Images x_1 are normalized to range $[-1, 1]$.

Implementation details. We trained our own continuous-time conditional VP-SDE model, and conditional Optimal Transport (conditional OT) flow model from scratch on the above datasets following the hyperparameters and training procedure outlined in Song et al. (2021c) and Lipman et al. (2022). These models are conditioned on class labels, not noisy images. All derivations hold with class label c since $q(y|c, x_1) = q(y|x_1)$ (i.e. the noisy image is independent of class label given the image). We use the open-source implementation of the Euler method provided in torchdiffEq library (Chen, 2018) to solve the ODE in our experiments. Our choice of Euler is intentionally simple, as we focus on flow sampling with the conditional OT path, and not on the choice of ODE solver.

Metrics. We follow prior works (Chung et al., 2022a; Kavar et al., 2022) and report Fréchet Inception Distance (FID) (Heusel et al., 2017), Learned Perceptual Image Patch Similarity (LPIPS) (Zhang et al., 2018), peak signal-to-noise ratio (PSNR), and structural similarity index (SSIM). We use open-source implementations of these metrics in the TorchMetrics library (Dettelsen et al., 2022).

Methods and baselines. We use our two pretrained model checkpoints—a conditional OT flow model and continuous VP-SDE diffusion model, and perform flow sampling with both conditional OT and Variance-Preserving (VP) paths, labeling our methods as OT-ODE and VP-ODE respectively. Because qualitative results are identical and quantitative results similar, we only include the VP-SDE diffusion model in the main text, and include the conditional OT flow model in Appendix D. We compare our OT-ODE and VP-ODE methods against IIGDM (Song et al., 2022) and RED-Diff (Mardani et al., 2023) as relevant baselines. We selected these baselines because they achieve state-of-the-art performance in solving linear inverse problems using diffusion models. The code for both baseline methods is available on github, and we make minimal changes while reimplementing these methods in our codebase. A fair comparison between methods requires considering the number of function evaluations (NFEs) used during sampling. We utilize at most 100 NFEs for our OT-ODE and VP-ODE sampling (see Appendix D), and utilize 100 for IIGDM as recommended in Song et al. (2022). We allow RED-Diff 1000 NFEs since it does not require gradients of \widehat{x}_1 . For OT-ODE following Algorithm 1, we use $\gamma_t = 1$ and initial $t = 0.2$ for all datasets and tasks. For VP-ODE following Algorithm 2 in the Appendix, we use $\gamma_t = \sqrt{\frac{\alpha_t}{\alpha_t^2 + \sigma_t^2}}$ and initial $t = 0.4$ for all datasets and tasks. Ablations of these mildly tuned hyperparameters are shown in Appendix C. We extensively tuned hyperparameters for RED-Diff and IIGDM as described in Appendix F, including different hyperparameters per dataset and task.

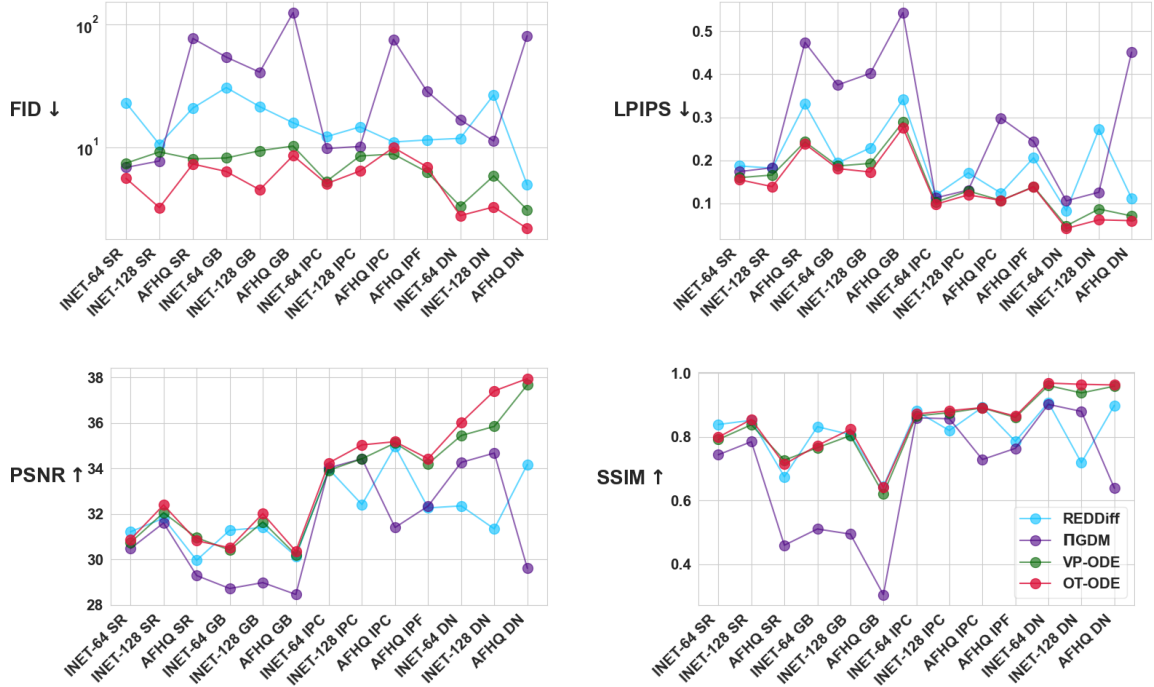


Figure 2: Quantitative evaluation of pretrained VP-SDE model for solving linear inverse problems on super-resolution (SR), gaussian deblurring (GB), inpainting with centered (IPC) and freeform mask (IPF), and denoising (DN) with $\sigma_y = 0.05$. We present results on face-blurred ImageNet-64 (INET-64), face-blurred ImageNet-128 (INET-128), and AFHQ.

4.1 Experimental Results

We report quantitative results for the VP-SDE model, across all datasets and linear measurements, in Figure 2 for $\sigma_y = 0.05$, and in Figure 9 within Appendix D for $\sigma_y = 0$. Additionally, we report results for the conditional OT flow model in Figure 11 and Figure 10 for $\sigma_y = 0.05$ and $\sigma_y = 0$, respectively, in Appendix D. Exact numerical values for all the metrics across all datasets and tasks can also be found in Appendix D. Qualitative images have been selected for demonstration purposes.

Gaussian deblurring. We report qualitative noisy results for the VP-SDE model in Figure 3 and for the conditional OT flow (cond-OT) model in Figure 12. We observe that OT-ODE and VP-ODE outperforms Π GDM and RED-Diff, both qualitatively and quantitatively, across all datasets for $\sigma_y = 0.05$. As shown in these figures, Π GDM tends to sharpen the images, which sometimes results in unnatural textures in the images. Further, we also observe some unnatural textures and background noise with RED-Diff for $\sigma_y = 0.05$. For $\sigma_y = 0$, OT-ODE has better FID and LPIPS, but Π GDM shows improved PSNR and SSIM. Figure 21 and Figure 18 show qualitative examples for $\sigma_y = 0$.

Super-resolution. We report qualitative noisy results for the VP-SDE model in Figure 4 and for the cond-OT model in Figure 13. OT-ODE consistently achieves better FID, LPIPS and PSNR metrics compared to other methods for $\sigma_y = 0.05$ (See Figure 2 and 11). Similar to Gaussian deblurring, Π GDM tends to produce sharper edges. This is certainly desirable to achieve good super-resolution, but sometimes this results in unnatural textures in the images (See Figure 4). RED-Diff for $\sigma_y = 0.05$ gives slightly blurry images. In our experiments, we observe RED-Diff is sensitive to the values of σ_y , and we get good quality results for smaller values of σ_y , but the performance deteriorates with increase in value of σ_y . For $\sigma_y = 0$, as shown in Figure 19 and Figure 22, all the methods achieve comparable performance and the method declared best varies per metric and dataset.

Inpainting. For centered mask inpainting, OT-ODE outperforms Π GDM and RED-Diff in terms of LPIPS, PSNR and SSIM across all datasets at $\sigma_y = 0.05$. Regarding FID, OT-ODE performs comparably to or better than VP-ODE (See Figure 2 and 11). Similar observations hold true for inpainting with freeform mask on AFHQ. We present qualitative

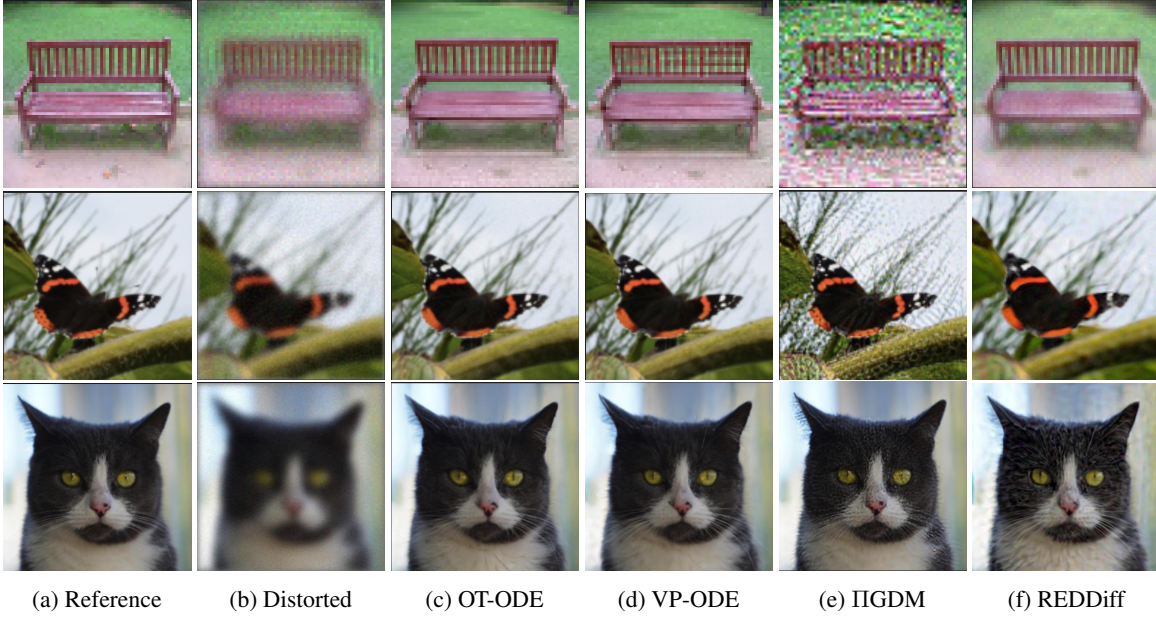


Figure 3: Results for Gaussian deblurring with VP-SDE model and $\sigma_y = 0.05$ for **(first row)** ImageNet-64, **(second row)** ImageNet-128, and **(third row)** AFHQ.

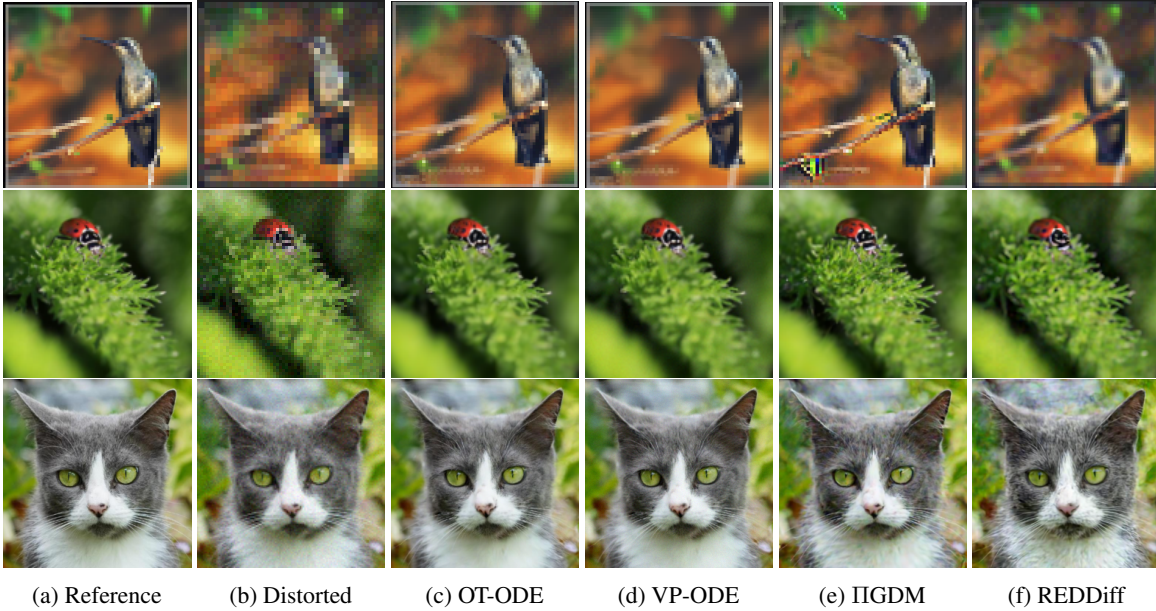


Figure 4: Results for super-resolution with VP-SDE model and $\sigma_y = 0.05$ for **(first row)** ImageNet-64 $2\times$, **(second row)** ImageNet-128 $2\times$, and **(third row)** AFHQ $4\times$.

noisy results for the VP-SDE model in Figure 5 and the cond-OT model in Figure 14. As evident in these images, OT-ODE can result in more semantically meaningful inpainting (for instance, the shape of bird’s neck, and shape of hot-dog bread in Figure 5). In contrast, the inpainted regions generated by RED-Diff tend to be blurry and less semantically meaningful. However, we note that OT-ODE (and VP-ODE) inpainting occasionally produces artifacts in the inpainted region as the resolution of image increases. We show examples of such negative inpainting results in Appendix D.2. Empirically, we observe that performance of RED-Diff and IIGDM improves as σ_y decreases. For $\sigma_y = 0$, RED-Diff achieves higher PSNR and SSIM, but performs worse than OT-ODE in terms of FID and LPIPS (Refer to Figure 9). OT-ODE’s tendency to produce inpainting artifacts for higher resolution images remains for $\sigma_y = 0$, and can occur

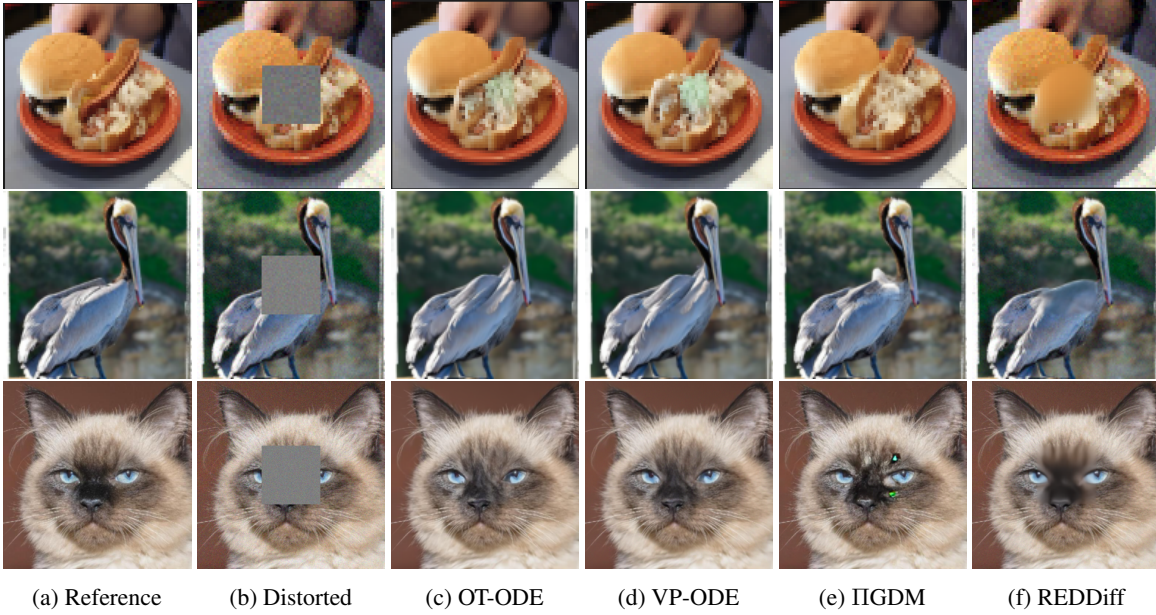


Figure 5: Results for inpainting (centered mask) with VP-SDE model and $\sigma_y = 0.05$ for **(first row)** ImageNet-64, **(second row)** ImageNet-128, and **(third row)** AFHQ.

for the same images as $\sigma_y = 0.05$. These artifacts can significantly degrade the pixel-based metrics PSNR and SSIM more than the perceptual metrics such as FID and LPIPS. We further note that noiseless inpainting for OT-ODE can be improved by incorporating null-space decomposition (Wang et al., 2022). We describe this adjustment in Appendix E.

5 Related Work

The challenge of solving noisy linear inverse problems without any training has been tackled in many ways, often with other solution concepts than posterior sampling (Elad et al., 2023). Utilizing a diffusion model has a host of recent research that we build upon. Our state-of-the-art baselines IIGDM (Song et al., 2022) and RED-Diff (Mardani et al., 2023) correspond to lines of research in gradient-based corrections and variational inference.

Earlier gradient-based corrections that approximate $\nabla_{\mathbf{x}_t} \ln q(\mathbf{y}|\mathbf{x}_t)$ in various ways include Diffusion Posterior Sampling (DPS) (Chung et al., 2022a), Manifold Constrained Gradient (Chung et al., 2022b), and an annealed approximation (Jalal et al., 2021). IIGDM out-performs earlier methods combining adaptive weights and Gaussian posterior approximation with discrete-time denoising diffusion implicit model (DDIM) sampling (Song et al., 2021a). Here we adapt IIGDM to all Gaussian probability paths and to flow sampling. Our results show adaptive weights are unnecessary for strongly performing conditional OT flow sampling. Denoising Diffusion Null Models (DDNM) (Wang et al., 2022) proposed an alternative approximation of $\mathbb{E}_q[\mathbf{x}_1|\mathbf{x}_t, \mathbf{y}]$ using a null-space decomposition specific to linear inverse problems, which has been explored in combination with our method in Appendix E.

RED-Diff (Mardani et al., 2023) approximates intractable $q(\mathbf{x}_1|\mathbf{y})$ directly using variational inference, solving for parameters via optimization. RED-Diff was reported to have mode-seeking behavior confirmed by our results where RED-Diff performed better for noiseless inference. Another earlier variational inference method is Denoising Diffusion Restoration Models (DDRM) (Kawar et al., 2022). DDRM showed SVD can be memory-efficient for image applications, and we adapt their SVD implementations for super-resolution and blur. DDRM incorporates noiseless method ILVR (Choi et al., 2021), and leverages a measurement-dependent forward process (i.e. $q(\mathbf{x}_t|\mathbf{y}, \mathbf{x}_1) \neq q(\mathbf{x}_t|\mathbf{x}_1)$) like earlier SNIPS (Kawar et al., 2021). SNIPS collapses in special cases to variants proposed in Song & Ermon (2019); Song et al. (2021c); Kadkhodaie & Simoncelli (2020) for linear inverse problems.

6 Discussion, Limitations, and Future work

We have presented a training-free approach to solve linear inverse problems using flows that can leverage either pretrained diffusion or flow models. The algorithm is simple, stable, and requires no hyperparameter tuning when used with conditional OT probability paths. Our method combines past ideas from diffusion including IIGDM and early starting with the conditional OT probability path from flows, and our results demonstrate that this combination can solve inverse problems for both noisy and noiseless cases across a variety of datasets. Our algorithm using the conditional OT path (OT-ODE) produced results superior to the VP path (VP-ODE) and also to IIGDM and REDDiff for noisy inverse problems. For the noiseless case, the perceptual quality from OT-ODE is on par with IIGDM for super-resolution and gaussian deblurring, but lagging for inpainting due to image artifacts.

Another important limitation, shared with most of the past related research, is a restriction to linear observations with scalar variance. Our method can extend to arbitrary covariance, but non-linear observations are more complex. Non-linear observations occur with image inverse tasks when utilizing latent, not pixel-space, diffusion or flow models. Applying our approach to such measurements requires devising an alternative $q^{app}(\mathbf{y}|\mathbf{x}_t)$. Another shared limitation is that we consider the non-blind setting with known \mathbf{A} and σ_y .

Future research could tackle these limitations. For non-linear observations in latent space, we could perhaps build upon Rout et al. (2023) that uses a latent diffusion model for linear inverses. For the blind setting, we might start from blind extensions to DPS and DDRM (Chung et al., 2023; Murata et al., 2023). As demonstrated here, we may be able to adapt and possibly improve these approaches via conversion to flow sampling using conditional OT paths.

References

- Michael S Albergo and Eric Vanden-Eijnden. Building normalizing flows with stochastic interpolants. *arXiv preprint arXiv:2209.15571*, 2022. 2, 3
- Ricky T. Q. Chen. torchdiffeq, 2018. URL <https://github.com/rtqichen/torchdiffeq>. 6
- Ricky TQ Chen, Yulia Rubanova, Jesse Bettencourt, and David K Duvenaud. Neural ordinary differential equations. *Advances in neural information processing systems*, 31, 2018a. 45
- Ricky TQ Chen, Yulia Rubanova, Jesse Bettencourt, and David K Duvenaud. Neural ordinary differential equations. *Advances in neural information processing systems*, 31, 2018b. 2, 3
- Jooyoung Choi, Sungwon Kim, Yonghyun Jeong, Youngjune Gwon, and Sungroh Yoon. Ilvr: Conditioning method for denoising diffusion probabilistic models. *arXiv preprint arXiv:2108.02938*, 2021. 9
- Yunjey Choi, Youngjung Uh, Jaejun Yoo, and Jung-Woo Ha. Stargan v2: Diverse image synthesis for multiple domains. In *Proceedings of the IEEE Conference on Computer Vision and Pattern Recognition*, 2020. 5
- Hyungjin Chung, Jeongsol Kim, Michael T Mccann, Marc L Klasky, and Jong Chul Ye. Diffusion posterior sampling for general noisy inverse problems. *arXiv preprint arXiv:2209.14687*, 2022a. 2, 4, 6, 9
- Hyungjin Chung, Byeongsu Sim, Dohoon Ryu, and Jong Chul Ye. Improving diffusion models for inverse problems using manifold constraints. *arXiv preprint arXiv:2206.00941*, 2022b. 9
- Hyungjin Chung, Byeongsu Sim, and Jong Chul Ye. Come-closer-diffuse-faster: Accelerating conditional diffusion models for inverse problems through stochastic contraction. In *Proceedings of the IEEE/CVF Conference on Computer Vision and Pattern Recognition*, pp. 12413–12422, 2022c. 5
- Hyungjin Chung, Jeongsol Kim, Sehui Kim, and Jong Chul Ye. Parallel diffusion models of operator and image for blind inverse problems. In *Proceedings of the IEEE/CVF Conference on Computer Vision and Pattern Recognition (CVPR)*, pp. 6059–6069, June 2023. 10
- Jia Deng, Wei Dong, Richard Socher, Li-Jia Li, Kai Li, and Li Fei-Fei. Imagenet: A large-scale hierarchical image database. In *2009 IEEE conference on computer vision and pattern recognition*, pp. 248–255. Ieee, 2009. 5

- Nicki Skafted Detlefsen, Jiri Borovec, Justus Schock, Ananya Harsh Jha, Teddy Koker, Luca Di Liello, Daniel Stancil, Changsheng Quan, Maxim Grechkin, and William Falcon. Torchmetrics-measuring reproducibility in pytorch. *Journal of Open Source Software*, 7(70):4101, 2022. [6](#)
- Michael Elad, Bahjat Kawar, and Gregory Vaksman. Image denoising: The deep learning revolution and beyond—a survey paper. *SIAM Journal on Imaging Sciences*, 16(3):1594–1654, 2023. [9](#)
- Will Grathwohl, Ricky TQ Chen, Jesse Bettencourt, Ilya Sutskever, and David Duvenaud. Ffjord: Free-form continuous dynamics for scalable reversible generative models. *arXiv preprint arXiv:1810.01367*, 2018. [45](#)
- Martin Heusel, Hubert Ramsauer, Thomas Unterthiner, Bernhard Nessler, and Sepp Hochreiter. Gans trained by a two time-scale update rule converge to a local nash equilibrium. *Advances in neural information processing systems*, 30, 2017. [6](#)
- Jonathan Ho, Ajay Jain, and Pieter Abbeel. Denoising diffusion probabilistic models. *Neural Information Processing Systems (NeurIPS)*, 2020. [2](#), [3](#)
- Ajil Jalal, Marius Arvinte, Giannis Daras, Eric Price, Alexandros G Dimakis, and Jon Tamir. Robust compressed sensing mri with deep generative priors. *Advances in Neural Information Processing Systems*, 34:14938–14954, 2021. [9](#)
- Zahra Kadhodaie and Eero P Simoncelli. Solving linear inverse problems using the prior implicit in a denoiser. *arXiv preprint arXiv:2007.13640*, 2020. [9](#)
- Tero Karras, Miika Aittala, Timo Aila, and Samuli Laine. Elucidating the design space of diffusion-based generative models. *Advances in Neural Information Processing Systems*, 35:26565–26577, 2022. [2](#), [4](#)
- Bahjat Kawar, Gregory Vaksman, and Michael Elad. Snips: Solving noisy inverse problems stochastically. *Advances in Neural Information Processing Systems*, 34:21757–21769, 2021. [9](#)
- Bahjat Kawar, Michael Elad, Stefano Ermon, and Jiaming Song. Denoising diffusion restoration models. *Advances in Neural Information Processing Systems*, 35:23593–23606, 2022. [6](#), [9](#)
- Diederik Kingma, Tim Salimans, Ben Poole, and Jonathan Ho. Variational diffusion models. *Advances in neural information processing systems*, 34:21696–21707, 2021. [3](#)
- Diederik P. Kingma and Ruiqi Gao. Vdm++: Variational diffusion models for high-quality synthesis, 2023. [3](#)
- Shanchuan Lin, Bingchen Liu, Jiashi Li, and Xiao Yang. Common diffusion noise schedules and sample steps are flawed. *arXiv preprint arXiv:2305.08891*, 2023. [3](#)
- Yaron Lipman, Ricky TQ Chen, Heli Ben-Hamu, Maximilian Nickel, and Matt Le. Flow matching for generative modeling. *arXiv preprint arXiv:2210.02747*, 2022. [2](#), [3](#), [6](#), [13](#), [45](#)
- Xingchao Liu, Chengyue Gong, and Qiang Liu. Flow straight and fast: Learning to generate and transfer data with rectified flow. *arXiv preprint arXiv:2209.03003*, 2022. [2](#), [3](#)
- Morteza Mardani, Jiaming Song, Jan Kautz, and Arash Vahdat. A variational perspective on solving inverse problems with diffusion models. *arXiv preprint arXiv:2305.04391*, 2023. [2](#), [6](#), [9](#), [41](#)
- Robert J McCann. A convexity principle for interacting gases. *Advances in mathematics*, 128(1):153–179, 1997. [2](#)
- Naoki Murata, Koichi Saito, Chieh-Hsin Lai, Yuhta Takida, Toshimitsu Uesaka, Yuki Mitsufuji, and Stefano Ermon. Gibbsddrm: A partially collapsed gibbs sampler for solving blind inverse problems with denoising diffusion restoration, 2023. [10](#)
- Herbert E Robbins. An empirical bayes approach to statistics. In *Breakthroughs in Statistics: Foundations and basic theory*, pp. 388–394. Springer, 1992. [3](#)
- Litu Rout, Negin Raoof, Giannis Daras, Constantine Caramanis, Alexandros G Dimakis, and Sanjay Shakkottai. Solving linear inverse problems provably via posterior sampling with latent diffusion models. *arXiv preprint arXiv:2307.00619*, 2023. [10](#)

- Olga Russakovsky, Jia Deng, Hao Su, Jonathan Krause, Sanjeev Satheesh, Sean Ma, Zhiheng Huang, Andrej Karpathy, Aditya Khosla, Michael Bernstein, et al. Imagenet large scale visual recognition challenge. *International journal of computer vision*, 115:211–252, 2015. [5](#)
- Chitwan Saharia, William Chan, Huiwen Chang, Chris Lee, Jonathan Ho, Tim Salimans, David Fleet, and Mohammad Norouzi. Palette: Image-to-image diffusion models. In *ACM SIGGRAPH 2022 Conference Proceedings*, pp. 1–10, 2022a. [2](#), [6](#)
- Chitwan Saharia, Jonathan Ho, William Chan, Tim Salimans, David J Fleet, and Mohammad Norouzi. Image super-resolution via iterative refinement. *IEEE Transactions on Pattern Analysis and Machine Intelligence*, 45(4):4713–4726, 2022b. [2](#)
- Neta Shaul, Ricky TQ Chen, Maximilian Nickel, Matthew Le, and Yaron Lipman. On kinetic optimal probability paths for generative models. In *International Conference on Machine Learning*, pp. 30883–30907. PMLR, 2023. [2](#), [3](#)
- Jascha Sohl-Dickstein, Eric Weiss, Niru Maheswaranathan, and Surya Ganguli. Deep unsupervised learning using nonequilibrium thermodynamics. In *International Conference on Machine Learning (ICML)*, 2015. [2](#)
- Jiaming Song, Chenlin Meng, and Stefano Ermon. Denoising diffusion implicit models. In *International Conference on Learning Representations (ICLR)*, 2021a. [2](#), [9](#)
- Jiaming Song, Arash Vahdat, Morteza Mardani, and Jan Kautz. Pseudoinverse-guided diffusion models for inverse problems. In *International Conference on Learning Representations*, 2022. [2](#), [4](#), [5](#), [6](#), [9](#), [40](#)
- Yang Song and Stefano Ermon. Generative modeling by estimating gradients of the data distribution. *Neural Information Processing Systems (NeurIPS)*, 2019. [2](#), [3](#), [9](#)
- Yang Song, Conor Durkan, Iain Murray, and Stefano Ermon. Maximum likelihood training of score-based diffusion models. *Advances in Neural Information Processing Systems*, 34:1415–1428, 2021b. [3](#)
- Yang Song, Jascha Sohl-Dickstein, Diederik P Kingma, Abhishek Kumar, Stefano Ermon, and Ben Poole. Score-based generative modeling through stochastic differential equations. In *International Conference on Learning Representations (ICLR)*, 2021c. [2](#), [3](#), [4](#), [6](#), [9](#)
- Yinhui Wang, Jiwen Yu, and Jian Zhang. Zero-shot image restoration using denoising diffusion null-space model. *arXiv preprint arXiv:2212.00490*, 2022. [2](#), [9](#), [35](#)
- Kaiyu Yang, Jacqueline H Yau, Li Fei-Fei, Jia Deng, and Olga Russakovsky. A study of face obfuscation in imagenet. In *International Conference on Machine Learning*, pp. 25313–25330. PMLR, 2022. [5](#)
- Richard Zhang, Phillip Isola, Alexei A Efros, Eli Shechtman, and Oliver Wang. The unreasonable effectiveness of deep features as a perceptual metric. In *CVPR*, 2018. [6](#)

A Proofs

For clarity, we restate Theorems and Lemmas from the main text before giving their proof.

Lemma 1. *For Gaussian probability path q given by Eq. 5, the optimal solution for $\hat{v}(\mathbf{x}_t, \mathbf{y})$ is known given $\mathbb{E}_q[\mathbf{x}_1|\mathbf{x}_t, \mathbf{y}]$, and vice versa.*

Proof. Inserting Gaussian probability paths defined by Eq. 5 into Eq. 4 gives

$$\mathbb{E}_q \left[\frac{d\mathbf{x}_t}{dt} \middle| \mathbf{x}_t, \mathbf{y}, \mathbf{x}_1 \right] = \frac{d\alpha_t}{dt} \mathbf{x}_1 + \frac{d\sigma_t}{dt} \left(\frac{\mathbf{x}_t - \alpha_t \mathbf{x}_1}{\sigma_t} \right). \quad (15)$$

So we reparameterize vector field $\hat{v}(\mathbf{x}_t, \mathbf{y}) = \frac{d\alpha_t}{dt} \hat{\mathbf{x}}_1(\mathbf{x}_t, \mathbf{y}) + \frac{d\sigma_t}{dt} \left(\frac{\mathbf{x}_t - \alpha_t \hat{\mathbf{x}}_1(\mathbf{x}_t, \mathbf{y})}{\sigma_t} \right)$. Inserting these expressions into the Conditional Flow Matching loss gives

$$\int_0^1 \left(\alpha_t \frac{d \ln(\alpha_t / \sigma_t)}{dt} \right)^2 \mathbb{E}_q[(\hat{\mathbf{x}}_1 - \mathbf{x}_1)^2] dt, \quad (16)$$

recovering the denoising loss with particular $w(t)$. The optimal solution does not depend on the weights and is $\mathbb{E}_q[\mathbf{x}_1|\mathbf{x}_t, \mathbf{y}]$. \square

Lemma 2. *Consider two Gaussian probability paths q and q' defined by Eq. 5 with α_t, σ_t and α'_t, σ'_t respectively. Define $t'(t)$ as the unique solution to $\frac{\sigma_t}{\alpha_t} = \frac{\sigma'_{t'}}{\alpha'_{t'}}$ when it exists for given t . Then*

$$\mathbb{E}_q[\mathbf{x}_1|\mathbf{x}_t, \mathbf{y}] = \mathbb{E}_{q'}[\mathbf{x}_1|\mathbf{X}'_{t'(t)} = \alpha'_{t'(t)} \mathbf{x}_t / \alpha_t, \mathbf{y}]. \quad (9)$$

Proof. We first note that q and q' share $q(\mathbf{x}_1|\mathbf{y}) = q'(\mathbf{x}_1|\mathbf{y})$. Then algebraically for Gaussian distributions q and q' , $q(\mathbf{X}_t = \mathbf{x}_t|\mathbf{x}_1, \mathbf{y}) = q'(\mathbf{X}'_{t'(t)} = \alpha'_{t'(t)} \mathbf{x}_t / \alpha_t|\mathbf{x}_1, \mathbf{y})$ when $t'(t)$ exists. The solution for $t'(t)$ is unique due to the monotonicity requirements of both α and σ . Since the joint densities are therefore identical, $\mathbb{E}_q[\mathbf{x}_1|\mathbf{x}_t, \mathbf{y}] = \mathbb{E}_{q'}[\mathbf{x}_1|\mathbf{X}'_{t'(t)} = \alpha'_{t'(t)} \mathbf{x}_t / \alpha_t, \mathbf{y}]$. \square

Theorem 1. *Let q be a Gaussian probability path described by Eq. 5. Assume we observe $\mathbf{y} \sim q(\mathbf{y}|\mathbf{x}_1)$ for arbitrary $q(\mathbf{y}|\mathbf{x}_1)$ and $v(\mathbf{x}_t)$ is a vector field enabling sampling $\mathbf{x}_t \sim q(\mathbf{x}_t)$. Then a vector field $v(\mathbf{x}_t, \mathbf{y})$ enabling sampling $\mathbf{x}_t \sim q(\mathbf{x}_t|\mathbf{y})$ can be written*

$$v(\mathbf{x}_t, \mathbf{y}) = v(\mathbf{x}_t) + \sigma_t^2 \frac{d \ln(\alpha_t / \sigma_t)}{dt} \nabla_{\mathbf{x}_t} \ln q(\mathbf{y}|\mathbf{x}_t). \quad (11)$$

Proof. The optimal $v(\mathbf{x}_t, \mathbf{y})$ for the Conditional Flow Matching loss is $\mathbb{E}_q[\frac{d\mathbf{x}_t}{dt}|\mathbf{x}_t, \mathbf{y}]$ and for Gaussian probability paths described by Eq. 5 can be written using Eq. 15 as

$$v(\mathbf{x}_t, \mathbf{y}) = \frac{d\alpha_t}{dt} \mathbb{E}_q[\mathbf{x}_1|\mathbf{x}_t, \mathbf{y}] + \frac{d\sigma_t}{dt} \left(\frac{\mathbf{x}_t - \alpha_t \mathbb{E}_q[\mathbf{x}_1|\mathbf{x}_t, \mathbf{y}]}{\sigma_t} \right), \quad (17)$$

where the identical expression without \mathbf{y} holds for $v(\mathbf{x}_t)$. Inserting the result from Eq. 6 and simplifying gives Eq. 11. \square

B Our method for any Gaussian probability path

Algorithm 1 in the main text is specific to conditional OT probability paths. Here we provide Algorithm 2 for any Gaussian probability path specified by Eq. 5. Algorithm 1 and Algorithm 2 are written assuming a denoiser $\hat{\mathbf{x}}_1(\mathbf{x}_t)$ is provided from a pretrained diffusion model. For completeness, we also include equivalent Algorithm 3 that assumes $\hat{v}(\mathbf{x}_t)$ is provided from a pretrained flow model. In all cases, the vector field or denoiser is evaluated only once per iteration.

Our VP-ODE sampling results correspond to α_t and σ_t given from the Variance-Preserving path, which can be found in (Lipman et al., 2022).

Algorithm 2 A training-free approach to solve inverse problems via flows with a pretrained denoiser

Require: Pretrained denoiser $\widehat{\mathbf{x}}_1(\mathbf{x}_t)$ converted to Gaussian probability path with α_t and σ_t using Section 3.1, noisy measurement \mathbf{y} , measurement matrix \mathbf{A} , initial time t , adaptive weights γ_t , and std σ_y

- 1: Initialize $\mathbf{x}_t = \alpha_t \mathbf{y} + \sigma_t \epsilon$, where $\epsilon \sim \mathcal{N}(0, \mathbf{I})$ ▷ Initialize \mathbf{x}_t , Eq. (14)
- 2: $\mathbf{z}_t = \mathbf{x}_t$
- 3: **for** each time step t' of ODE integration **do** ▷ Integrate ODE from $t' = t$ to 1.
- 4: $r_{t'}^2 = \frac{\sigma_{t'}^2}{\sigma_{t'}^2 + \alpha_{t'}^2}$ ▷ Value of r_t^2 from Eq. (13)
- 5: $\widehat{\mathbf{v}} = \left(\alpha_t \frac{d \ln(\alpha_t / \sigma_t)}{dt} \right) \widehat{\mathbf{x}}_1 + \frac{d \ln \sigma_t}{dt} \mathbf{z}_t$ ▷ Convert $\widehat{\mathbf{x}}_1$ to vector field, Eq. (8)
- 6: $\mathbf{g} = (\mathbf{y} - \mathbf{A} \widehat{\mathbf{x}}_1)^\top (r_{t'}^2 \mathbf{A} \mathbf{A}^\top + \sigma_y^2 \mathbf{I})^{-1} \mathbf{A} \frac{\partial \widehat{\mathbf{x}}_1}{\partial \mathbf{z}_{t'}}$ ▷ IIGDM correction
- 7: $\widehat{\mathbf{v}}_{\text{corrected}} = \widehat{\mathbf{v}} + \sigma_t^2 \frac{d \ln(\alpha_t / \sigma_t)}{dt} \gamma_t \mathbf{g}$ ▷ Correct unconditional vector field $\widehat{\mathbf{v}}$, Eq. (12)
- 8: **end for**

Algorithm 3 A training-free approach to solve inverse problems via flows with a pretrained vector field

Require: Pretrained vector field $\widehat{\mathbf{v}}(\mathbf{x}_t)$ converted to Gaussian probability path with α_t and σ_t using Section 3.1, noisy measurement \mathbf{y} , measurement matrix \mathbf{A} , initial time t , adaptive weights γ_t , and std σ_y

- 1: Initialize $\mathbf{x}_t = \alpha_t \mathbf{y} + \sigma_t \epsilon$, where $\epsilon \sim \mathcal{N}(0, \mathbf{I})$ ▷ Initialize \mathbf{x}_t , Eq. (14)
- 2: $\mathbf{z}_t = \mathbf{x}_t$
- 3: **for** each time step t' of ODE integration **do** ▷ Integrate ODE from $t' = t$ to 1.
- 4: $\widehat{\mathbf{v}} = \widehat{\mathbf{v}}(\mathbf{z}_{t'})$ ▷ $\mathbf{z}_{t'}$ is value of \mathbf{x}_t at time t' during ODE integration
- 5: $r_{t'}^2 = \frac{\sigma_{t'}^2}{\sigma_{t'}^2 + \alpha_{t'}^2}$ ▷ Value of r_t^2 from Eq. (13)
- 6: $\widehat{\mathbf{x}}_1 = \left(\alpha_t \frac{d \ln(\alpha_t / \sigma_t)}{dt} \right)^{-1} \left(\widehat{\mathbf{v}} - \frac{d \ln \sigma_t}{dt} \mathbf{z}_t \right)$ ▷ Convert vector field to $\widehat{\mathbf{x}}_1$, Eq. (8)
- 7: $\mathbf{g} = (\mathbf{y} - \mathbf{A} \widehat{\mathbf{x}}_1)^\top (r_{t'}^2 \mathbf{A} \mathbf{A}^\top + \sigma_y^2 \mathbf{I})^{-1} \mathbf{A} \frac{\partial \widehat{\mathbf{x}}_1}{\partial \mathbf{z}_{t'}}$ ▷ IIGDM correction
- 8: $\widehat{\mathbf{v}}_{\text{corrected}} = \widehat{\mathbf{v}} + \sigma_t^2 \frac{d \ln(\alpha_t / \sigma_t)}{dt} \gamma_t \mathbf{g}$ ▷ Correct unconditional vector field $\widehat{\mathbf{v}}$, Eq. (12)
- 9: **end for**

C Ablation Study

Choice of initialization. We initialize the flow at time $t > 0$ as $\mathbf{x}_t = \alpha_t \mathbf{y} + \sigma_t \epsilon$ (y-init) where $\epsilon \sim \mathcal{N}(0, \mathbf{I})$. Another choice of initialization is to use $\mathbf{x}_t = \alpha_t \mathbf{A}^\dagger \mathbf{y} + \sigma_t \epsilon$. However, empirically we find that this initialization performs worse than y-init on cond-OT model with OT-ODE sampling. We summarize the results of our ablation study in Table 1. We find that on Gaussian deblurring, initialization with $\mathbf{A}^\dagger \mathbf{y}$ does worse than y-init, while the performance of both the initializations is comparable for super-resolution. In all our experiments, we use y-init, due to its better performance on Gaussian deblurring.

Table 1: Quantitative evaluation of choice of initialization for conditional OT flow model with OT-ODE sampling on AFHQ dataset. We find that y-init outperforms $\mathbf{A}^\dagger \mathbf{y}$ on Gaussian deblurring.

Initialization	Start time	NFEs ↓	Gaussian deblur, $\sigma_y = 0.05$				SR 4×, $\sigma_y = 0.05$			
			FID ↓	LPIPS ↓	PSNR ↑	SSIM ↑	FID ↓	LPIPS ↓	PSNR ↑	SSIM ↑
y init	0.2	100	7.57	0.268	30.28	0.626	6.03	0.219	31.12	0.739
$\mathbf{A}^\dagger \mathbf{y}$	0.1	100	41.22	0.449	28.79	0.392	12.93	0.292	30.46	0.664
$\mathbf{A}^\dagger \mathbf{y}$	0.2	100	56.42	0.554	28.11	0.249	6.09	0.219	31.12	0.739

Ablation over γ_t for VP-ODE sampling. We compare the performance of $\gamma_t = 1$ against $\gamma_t = \sqrt{\frac{\alpha_t}{\alpha_t^2 + \sigma_t^2}}$. We show results of VP-ODE sampling with VP-SDE model in Table 2 and Table 3. As seen our choice of γ_t outperform $\gamma_t = 1$ across all the metrics on face-blurred ImageNet-128.

Table 2: Quantitative evaluation of value of γ_t in VP-ODE sampling with VP-SDE model on face-blurred ImageNet-128 dataset.

γ_t	Start time	NFEs ↓	SR 2×, $\sigma_y = 0.05$				Gaussian deblur, $\sigma_y = 0.05$			
			FID ↓	LPIPS ↓	PSNR ↑	SSIM ↑	FID ↓	LPIPS ↓	PSNR ↑	SSIM ↑
1	0.4	60	32.66	0.371	29.06	0.530	29.31	0.346	29.12	0.554
$\sqrt{\frac{\alpha_t}{\alpha_t^2 + \sigma_t^2}}$	0.4	60	9.14	0.167	32.06	0.838	10.14	0.196	31.59	0.800

Table 3: Quantitative evaluation of value of γ_t in VP-ODE sampling with VP-SDE model on face-blurred ImageNet-128 dataset.

γ_t	Start time	NFEs ↓	Inpainting-Center, $\sigma_y = 0.05$				Denoising, $\sigma_y = 0.05$			
			FID ↓	LPIPS ↓	PSNR ↑	SSIM ↑	FID ↓	LPIPS ↓	PSNR ↑	SSIM ↑
1	0.3	70	53.03	0.285	31.55	0.737	28.37	0.238	31.63	0.786
$\sqrt{\frac{\alpha_t}{\alpha_t^2 + \sigma_t^2}}$	0.3	70	8.47	0.129	34.43	0.876	5.83	0.087	35.85	0.938

Variation of performance with NFEs. We analyze the variation in performance of OT-ODE, VP-ODE and IIGDM for solving linear inverse problems as NFEs are varied. The results have been summarized in Figure 6. We observe that OT-ODE consistently outperforms VP-ODE and IIGDM across all measurements in terms of FID and LPIPS metrics, even for NFEs as small as 20. We also note that the choice of starting time matters to achieve good performance with OT-ODE. For instance, starting at $t = 0.4$ outperforms $t = 0.2$ when NFEs are small, but eventually as NFEs is increased, $t = 0.2$ performs better. We also note that IIGDM achieves higher values of PSNR and SSIM at smaller NFEs for super-resolution but has inferior FID and LPIPS compared to OT-ODE.

Choice of starting time. We plot the variation in performance of OT-ODE and VP-ODE sampling with change in start times for conditional OT model and VP-SDE model on AFHQ dataset in Figure 7 and Figure 8, respectively.

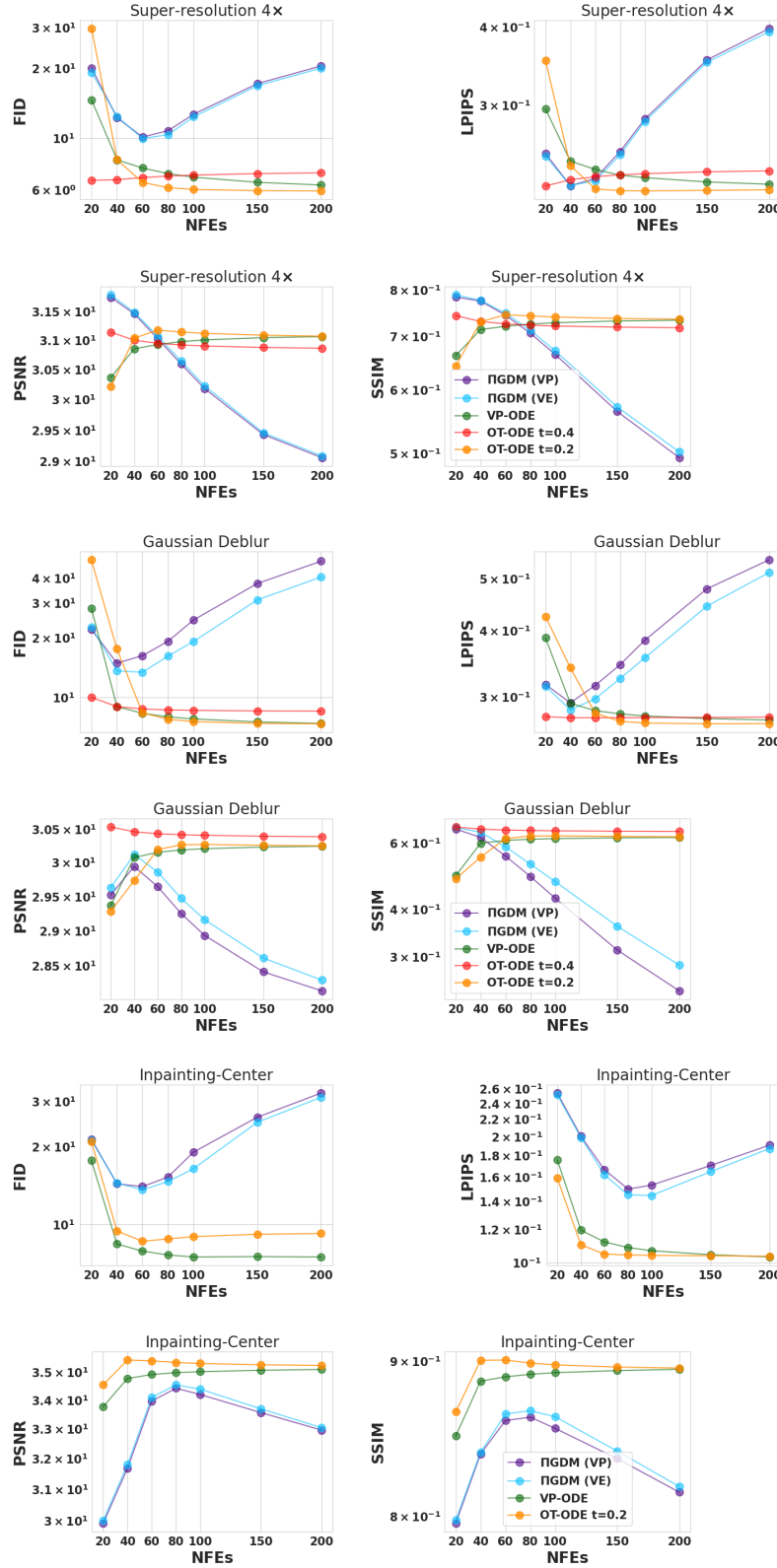


Figure 6: Performance of different procedures for solving linear inverse problems with variation in NFEs on AFHQ dataset. We use pretrained conditional OT model and set $\sigma_y = 0.05$. The legends VP and VE indicate the choice of r_t^2 used in IIGDM (See Appendix F.1). Time $t = 0.2$ and 0.4 indicates the starting time of sampling with OT-ODE.

We note that in general, OT-ODE sampling achieves optimal performance across all measurements and all metrics at $t = 0.2$ while VP-ODE sampling achieves optimal performance between start times of $t = 0.3$ and 0.4 . In this work, for all the experiments, we use $t = 0.2$ for OT-ODE sampling and $t = 0.4$ for VP-ODE sampling.

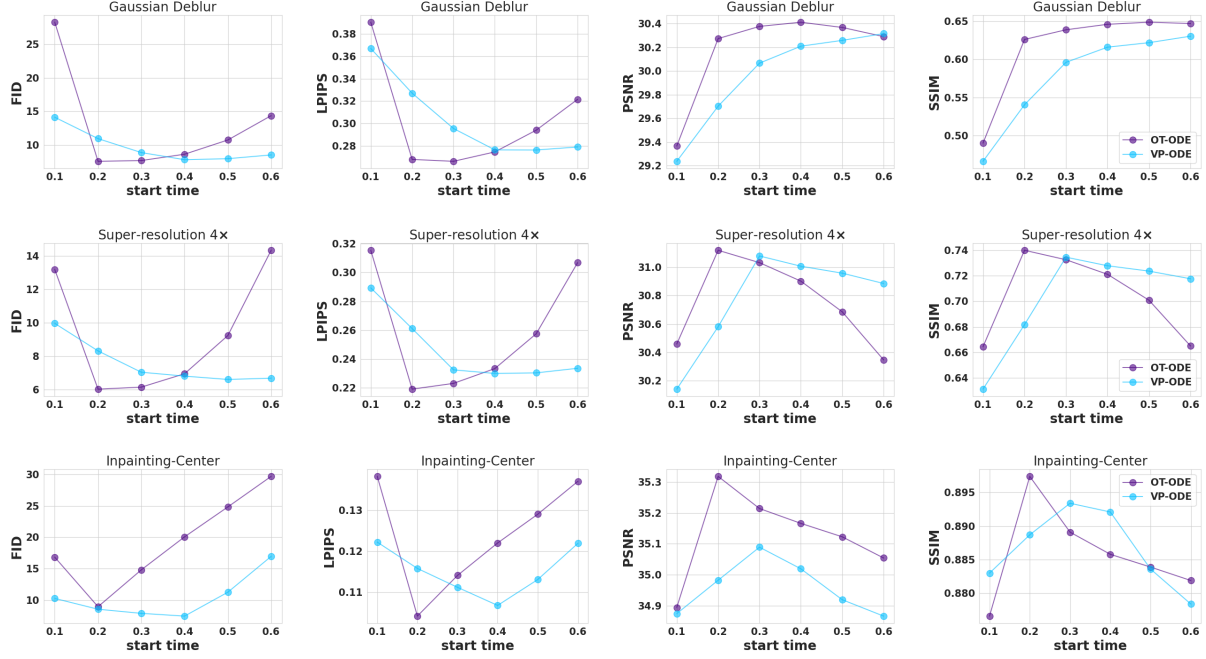


Figure 7: Performance of OT-ODE and VP-ODE in solving linear inverse problems with varying start times on AFHQ dataset. We use pretrained cond-OT model and set $\sigma_y = 0.05$.

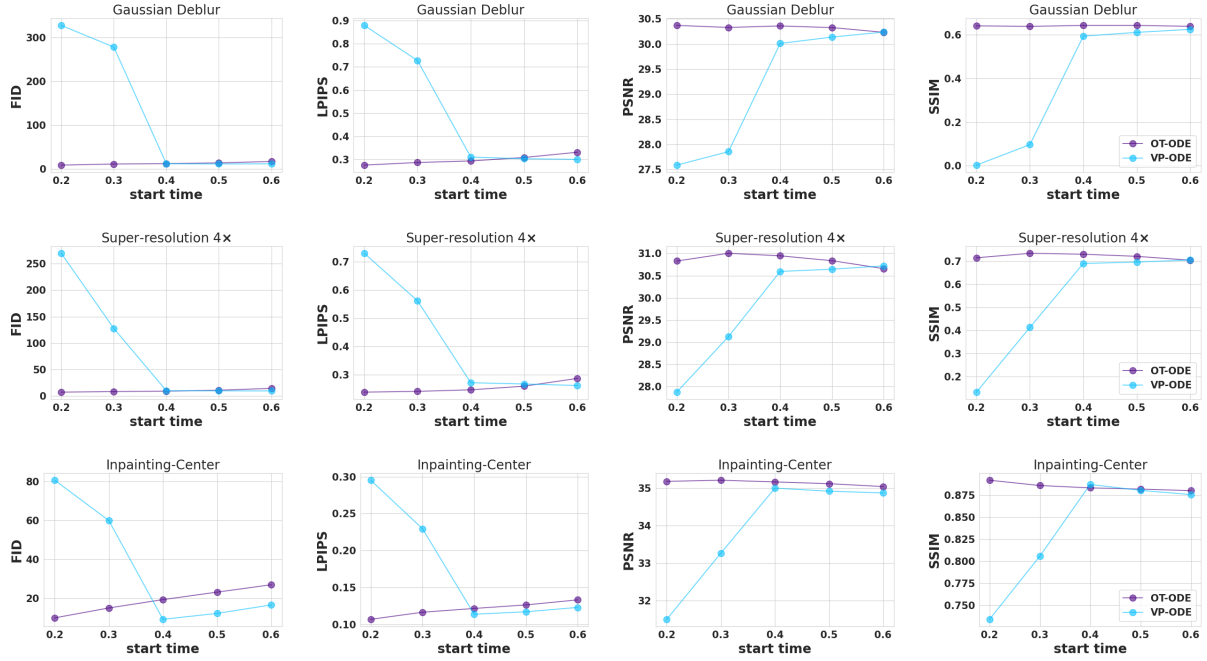


Figure 8: Performance of OT-ODE and VP-ODE in solving linear inverse problems with varying start times on AFHQ dataset. We use pretrained VP-SDE model and set $\sigma_y = 0.05$.

D Additional Empirical Results

The main text includes Figure 2 with $\sigma_y = 0.05$ produced with the denoiser from the continuous-time VP-SDE diffusion model showing plots of various metrics across all datasets and tasks. Here we provide the same for our pre-trained conditional OT flow matching model using Algorithm 3 in Figure 11, and noiseless figures for both models in Figure 9 and 10. To save compute, for the flow model we only include our IIGDM baseline as RED-Diff required extensive hyperparameter tuning. The qualitative results using the flow model instead of diffusion model checkpoint are identical.

This section also includes tables containing the numerical values of metrics across all datasets and tasks. The tables are hierarchically organized by noise, dataset, and task in consistent ordering. Noisy results with $\sigma_y = 0.05$ are in Table 4 to 9 and noiseless results with $\sigma_y = 0$ are in Table 8 to 13.

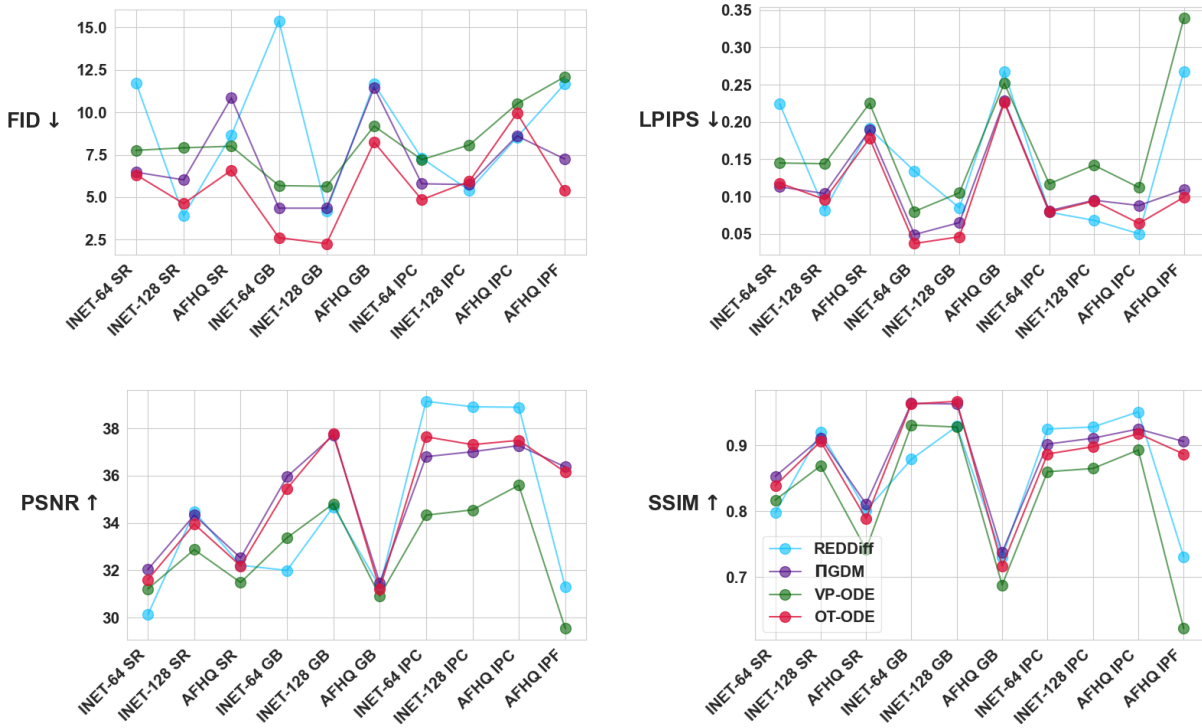


Figure 9: Quantitative evaluation of pretrained VP-SDE model for linear inverse problems on super-resolution (SR), gaussian deblurring (GB), image inpainting - centered mask (IPC) and inpainting - free-form (IPF) with $\sigma_y = 0$. We show results on face-blurred ImageNet-64 (INET-64), face-blurred ImageNet-128 (INET-128), and AFHQ-256 (AFHQ).

Table 4: Quantitative evaluation of linear inverse problems on face-blurred ImageNet-64 \times 64

Model	Inference	NFEs ↓	SR 2 \times , $\sigma_y = 0.05$				Gaussian deblur, $\sigma_y = 0.05$			
			FID ↓	LPIPS ↓	PSNR ↑	SSIM ↑	FID ↓	LPIPS ↓	PSNR ↑	SSIM ↑
OT	OT-ODE	80	6.07	0.157	30.88	0.799	6.83	0.185	30.51	0.773
OT	VP-ODE	80	7.82	0.163	30.75	0.792	8.72	0.190	30.40	0.765
OT	IIGDM	100	6.52	0.168	30.54	0.753	55.19	0.374	28.74	0.516
VP-SDE	OT-ODE	80	5.57	0.155	30.88	0.799	6.33	0.181	30.52	0.773
VP-SDE	VP-ODE	80	7.40	0.160	30.75	0.792	8.16	0.187	30.42	0.766
VP-SDE	IIGDM	100	6.84	0.174	30.48	0.743	54.77	0.376	28.74	0.511
VP-SDE	RED-Diff	1000	23.02	0.187	31.22	0.839	51.20	0.236	30.19	0.776

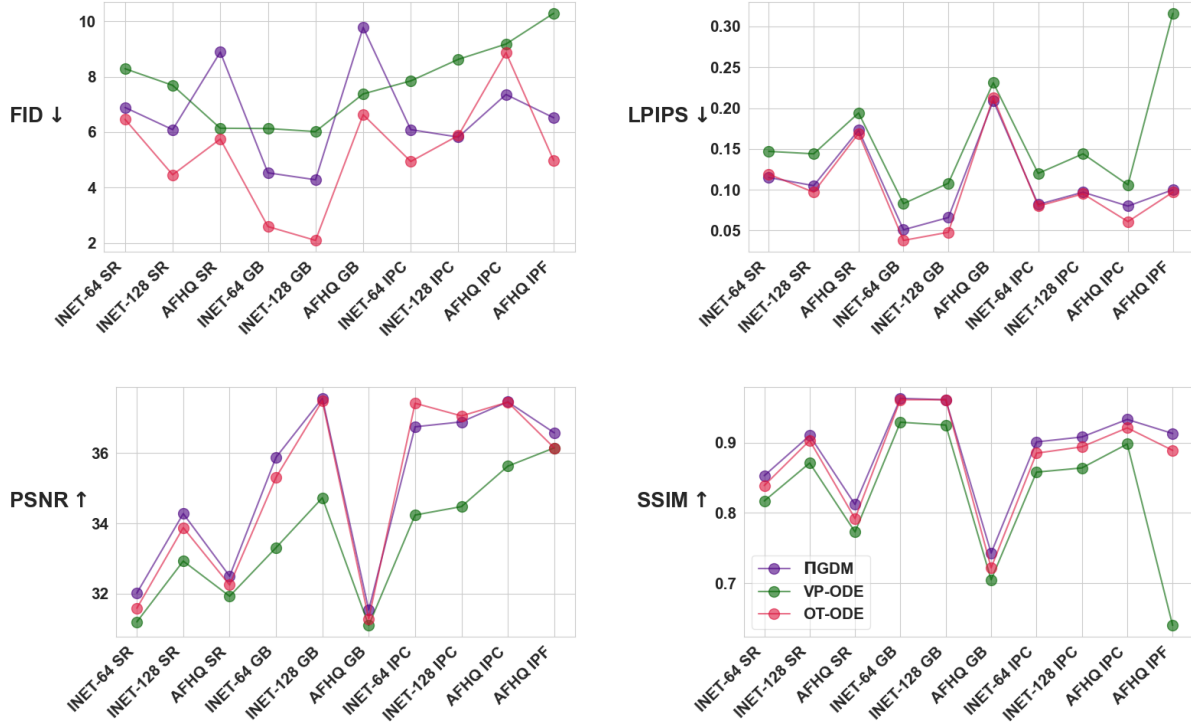


Figure 10: Quantitative evaluation of pretrained conditional OT model for linear inverse problems on super-resolution (SR), gaussian deblurring (GB), image inpainting - centered mask (IPC) and inpainting - freeform (IPF) with $\sigma_y = 0$. We show results on face-blurred ImageNet-64 (INET-64), face-blurred ImageNet-128 (INET-128), and AFHQ-256 (AFHQ).

Table 5: Quantitative evaluation of linear inverse problems on face-blurred ImageNet-64 \times 64

Model	Inference	NFEs ↓	Inpainting-Center, $\sigma_y = 0.05$				Denoising, $\sigma_y = 0.05$			
			FID ↓	LPIPS ↓	SSIM ↑	PSNR ↑	FID ↓	LPIPS ↓	SSIM ↑	PSNR ↑
OT	OT-ODE	80	5.45	0.101	34.21	0.870	2.91	0.044	35.96	0.968
OT	VP-ODE	80	5.70	0.105	33.87	0.865	3.54	0.049	35.37	0.960
OT	Π GDM	100	9.25	0.111	34.13	0.863	16.59	0.102	34.60	0.906
VP-SDE	OT-ODE	80	5.03	0.098	34.25	0.872	2.76	0.042	36.02	0.969
VP-SDE	VP-ODE	80	5.26	0.103	33.93	0.866	3.29	0.048	35.45	0.961
VP-SDE	Π GDM	100	9.75	0.113	34.03	0.860	17.19	0.107	34.25	0.901
VP-SDE	RED-Diff	1000	12.18	0.119	33.97	0.881	6.02	0.041	35.64	0.964

Table 6: Quantitative evaluation of linear inverse problems on face-blurred ImageNet-128 \times 128

Model	Inference	NFEs ↓	SR 2 \times , $\sigma_y = 0.05$				Gaussian deblur, $\sigma_y = 0.05$			
			FID ↓	LPIPS ↓	PSNR ↑	SSIM ↑	FID ↓	LPIPS ↓	PSNR ↑	SSIM ↑
OT	OT-ODE	70	3.22	0.141	32.35	0.820	4.84	0.175	31.94	0.821
OT	VP-ODE	70	7.52	0.162	32.24	0.847	8.49	0.191	31.76	0.809
OT	Π GDM	100	4.38	0.148	32.07	0.831	30.30	0.328	29.96	0.606
VP-SDE	OT-ODE	70	3.21	0.139	32.40	0.855	4.49	0.173	32.02	0.824
VP-SDE	VP-ODE	70	9.14	0.166	32.06	0.838	9.35	0.193	31.66	0.804
VP-SDE	Π GDM	100	7.55	0.183	31.61	0.785	55.61	0.463	28.57	0.414
VP-SDE	RED-Diff	1000	10.54	0.182	31.82	0.852	21.43	0.229	31.41	0.807

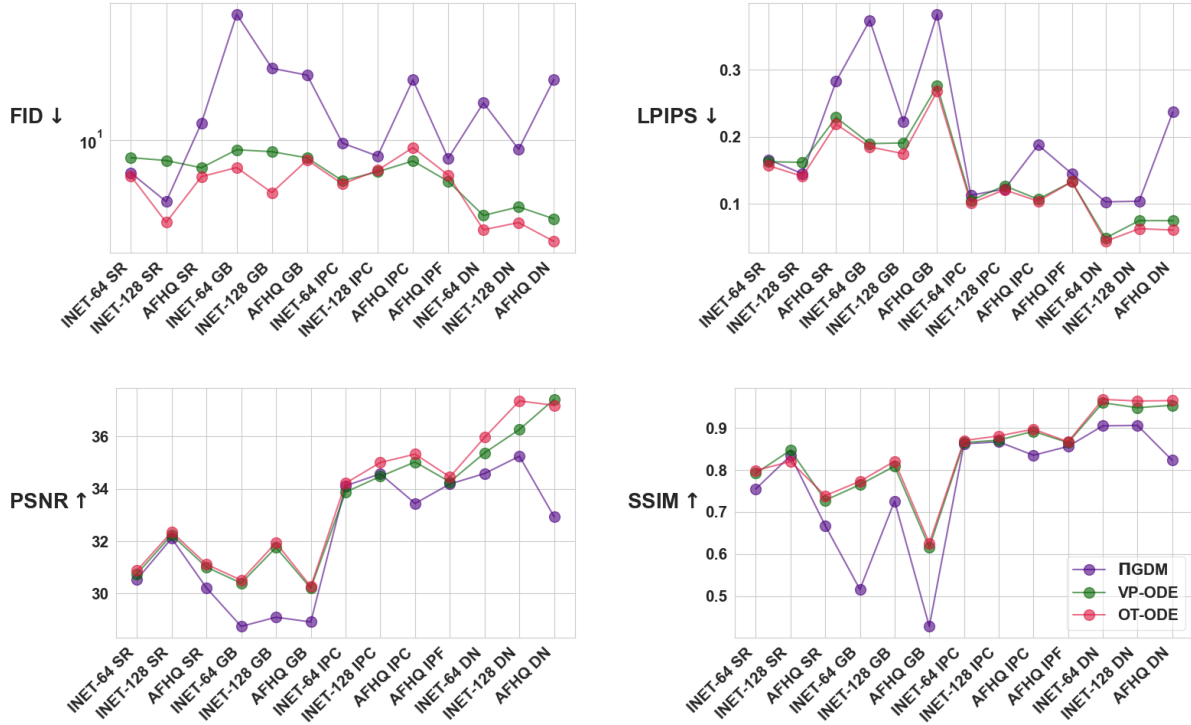


Figure 11: Quantitative evaluation of pretrained conditional OT model for linear inverse problems on super-resolution (SR), gaussian deblurring (GB), image inpainting - centered mask (IPC) and denoising (DN) with $\sigma_y = 0.05$. We show results on face-blurred ImageNet-64 (INET-64), face-blurred ImageNet-128 (INET-128), and AFHQ-256 (AFHQ).

Table 7: Quantitative evaluation of linear inverse problems on face-blurred ImageNet-128 \times 128

Model	Inference	NFEs \downarrow	Inpainting-Center, $\sigma_y = 0.05$				Denoising, $\sigma_y = 0.05$			
			FID \downarrow	LPIPS \downarrow	PSNR \uparrow	SSIM \uparrow	FID \downarrow	LPIPS \downarrow	PSNR \uparrow	SSIM \uparrow
OT	OT-ODE	70	6.58	0.121	35.00	0.881	3.21	0.063	37.35	0.964
OT	VP-ODE	70	6.44	0.127	34.47	0.871	3.98	0.075	36.26	0.948
OT	Π GDM	100	7.99	0.122	34.57	0.867	9.60	0.107	35.11	0.903
VP-SDE	OT-ODE	70	6.39	0.120	35.04	0.882	3.25	0.062	37.41	0.965
VP-SDE	VP-ODE	70	8.47	0.129	34.43	0.876	5.83	0.087	35.85	0.938
VP-SDE	Π GDM	100	9.75	0.130	34.45	0.858	10.69	0.124	34.72	0.882
VP-SDE	RED-Diff	1000	14.63	0.171	32.42	0.820	9.19	0.105	33.52	0.895

Table 8: Quantitative evaluation of linear inverse problems on AFHQ-256 \times 256

Model	Inference	NFEs \downarrow	SR 4 \times , $\sigma_y = 0.05$				Gaussian deblur, $\sigma_y = 0.05$			
			FID \downarrow	LPIPS \downarrow	PSNR \uparrow	SSIM \uparrow	FID \downarrow	LPIPS \downarrow	PSNR \uparrow	SSIM \uparrow
OT	OT-ODE	100	6.03	0.219	31.12	0.739	7.57	0.268	30.27	0.626
OT	VP-ODE	100	6.81	0.229	31.01	0.728	7.80	0.276	30.21	0.616
OT	Π GDM	100	12.69	0.285	30.18	0.665	24.60	0.383	28.93	0.429
VP-SDE	OT-ODE	100	7.28	0.238	30.83	0.714	8.53	0.276	30.37	0.641
VP-SDE	VP-ODE	100	8.02	0.243	30.96	0.727	10.21	0.289	30.21	0.621
VP-SDE	Π GDM	100	77.49	0.469	29.34	0.469	116.42	0.535	28.49	0.313
VP-SDE	RED-Diff	1000	20.84	0.331	29.97	0.675	15.81	0.341	30.15	0.645

Table 9: Quantitative evaluation of linear inverse problems on AFHQ-256 \times 256

Model	Inference	NFEs \downarrow	Inpainting-Center, $\sigma_y = 0.05$				Denoising, $\sigma_y = 0.05$			
			FID \downarrow	LPIPS \downarrow	PSNR \uparrow	SSIM \uparrow	FID \downarrow	LPIPS \downarrow	PSNR \uparrow	SSIM \uparrow
OT	OT-ODE	100	8.98	0.104	35.32	0.897	2.48	0.061	37.18	0.965
OT	VP-ODE	100	7.48	0.107	35.02	0.892	3.38	0.075	37.41	0.954
OT	IIGDM	100	19.09	0.153	34.20	0.855	22.87	0.237	32.93	0.823
VP-SDE	OT-ODE	100	9.93	0.107	35.18	0.892	2.17	0.060	37.95	0.963
VP-SDE	VP-ODE	100	8.78	0.107	35.12	0.891	3.08	0.071	37.68	0.959
VP-SDE	IIGDM	100	57.46	0.239	32.40	0.773	81.15	0.451	29.62	0.639
VP-SDE	RED-Diff	1000	11.02	0.124	34.97	0.893	4.93	0.112	34.18	0.899

Table 10: Quantitative evaluation of linear inverse problems on face-blurred ImageNet-64 \times 64

Model	Inference	NFEs \downarrow	SR 2 \times , $\sigma_y = 0$				Gaussian deblur, $\sigma_y = 0$			
			FID \downarrow	LPIPS \downarrow	PSNR \uparrow	SSIM \uparrow	FID \downarrow	LPIPS \downarrow	PSNR \uparrow	SSIM \uparrow
OT	OT-ODE	80	6.46	0.119	31.59	0.839	2.59	0.038	35.31	0.961
OT	VP-ODE	80	8.29	0.147	31.20	0.817	6.13	0.083	33.31	0.929
OT	IIGDM	100	6.89	0.115	32.02	0.853	4.53	0.051	35.88	0.963
VP-SDE	OT-ODE	80	6.32	0.118	31.60	0.839	2.61	0.037	35.45	0.963
VP-SDE	VP-ODE	80	7.76	0.145	31.21	0.817	5.68	0.080	33.37	0.931
VP-SDE	IIGDM	100	6.47	0.113	32.03	0.853	4.35	0.049	35.95	0.964
VP-SDE	RED-Diff	1000	11.74	0.224	30.12	0.798	15.39	0.134	31.99	0.879

Table 11: Quantitative evaluation of linear inverse problems on face-blurred ImageNet-64 \times 64

Model	Inference	NFEs \downarrow	Inpainting-Center, $\sigma_y = 0$			
			FID \downarrow	LPIPS \downarrow	PSNR \uparrow	SSIM \uparrow
OT	OT-ODE	80	4.94	0.080	37.42	0.885
OT	VP-ODE	80	7.85	0.120	34.24	0.858
OT	IIGDM	100	6.09	0.082	36.75	0.901
VP-SDE	OT-ODE	80	4.85	0.079	37.64	0.887
VP-SDE	VP-ODE	80	7.21	0.117	34.33	0.860
VP-SDE	IIGDM	100	5.79	0.081	36.81	0.902
VP-SDE	RED-Diff	1000	7.29	0.079	39.14	0.925

Table 12: Quantitative evaluation of linear inverse problems on face-blurred ImageNet-128 \times 128

Model	Inference	NFEs \downarrow	Inpainting-Center, $\sigma_y = 0$			
			FID \downarrow	LPIPS \downarrow	PSNR \uparrow	SSIM \uparrow
OT	OT-ODE	70	5.88	0.095	37.06	0.894
OT	VP-ODE	70	8.63	0.144	34.48	0.864
OT	IIGDM	100	5.82	0.097	36.89	0.908
VP-SDE	OT-ODE	70	5.93	0.094	37.31	0.898
VP-SDE	VP-ODE	70	8.08	0.142	34.55	0.865
VP-SDE	IIGDM	100	5.74	0.095	37.01	0.911
VP-SDE	RED-Diff	1000	5.40	0.068	38.91	0.928

Table 13: Quantitative evaluation of linear inverse problems on face-blurred ImageNet-128 \times 128

Model	Inference	NFEs \downarrow	SR $2\times$, $\sigma_y = 0$				Gaussian deblur, $\sigma_y = 0$			
			FID \downarrow	LPIPS \downarrow	PSNR \uparrow	SSIM \uparrow	FID \downarrow	LPIPS \downarrow	PSNR \uparrow	SSIM \uparrow
OT	OT-ODE	70	4.46	0.097	33.88	0.903	2.09	0.048	37.49	0.961
OT	VP-ODE	70	7.69	0.144	32.93	0.871	6.02	0.108	34.73	0.925
OT	Π GDM	100	6.09	0.105	34.28	0.910	4.28	0.066	37.56	0.961
VP-SDE	OT-ODE	70	4.62	0.096	33.95	0.906	2.26	0.046	37.79	0.967
VP-SDE	VP-ODE	70	7.91	0.144	32.87	0.869	5.64	0.105	34.81	0.928
VP-SDE	Π GDM	100	6.02	0.104	34.33	0.911	4.35	0.065	37.70	0.963
VP-SDE	RED-Diff	1000	3.90	0.082	34.47	0.92	4.19	0.085	34.68	0.929

Table 14: Quantitative evaluation of linear inverse problems on AFHQ-256 \times 256

Model	Inference	NFEs \downarrow	SR $4\times$, $\sigma_y = 0$				Gaussian deblur, $\sigma_y = 0$			
			FID \downarrow	LPIPS \downarrow	PSNR \uparrow	SSIM \uparrow	FID \downarrow	LPIPS \downarrow	PSNR \uparrow	SSIM \uparrow
OT	OT-ODE	100	5.75	0.169	32.25	0.792	6.63	0.213	31.29	0.722
OT	VP-ODE	100	6.14	0.194	31.93	0.773	7.38	0.231	31.10	0.705
OT	Π GDM	100	8.89	0.173	32.57	0.812	9.78	0.209	31.54	0.743
VP-SDE	OT-ODE	100	6.58	0.178	32.18	0.789	8.24	0.226	31.21	0.717
VP-SDE	VP-ODE	100	8.00	0.225	31.48	0.742	9.19	0.252	30.91	0.688
VP-SDE	Π GDM	100	10.85	0.189	32.52	0.811	11.46	0.228	31.47	0.738
VP-SDE	RED-Diff	1000	8.65	0.191	32.21	0.801	11.67	0.268	31.30	0.731

Table 15: Quantitative evaluation of linear inverse problems on AFHQ-256 \times 256

Model	Inference	NFEs \downarrow	Inpainting- <i>Center</i> , $\sigma_y = 0$				Inpainting- <i>Free-form</i> , $\sigma_y = 0$			
			FID \downarrow	LPIPS \downarrow	PSNR \uparrow	SSIM \uparrow	FID \downarrow	LPIPS \downarrow	PSNR \uparrow	SSIM \uparrow
OT	OT-ODE	100	8.87	0.061	37.45	0.921	4.98	0.097	36.15	0.889
OT	VP-ODE	100	9.18	0.106	35.63	0.898	6.92	0.135	34.72	0.869
OT	Π GDM	100	7.36	0.080	37.45	0.933	6.52	0.100	36.58	0.913
VP-SDE	OT-ODE	100	9.95	0.064	37.49	0.918	5.39	0.099	36.15	0.887
VP-SDE	VP-ODE	100	10.50	0.112	35.59	0.893	7.36	0.139	34.65	0.865
VP-SDE	Π GDM	100	8.61	0.088	37.27	0.925	7.25	0.109	36.37	0.906
VP-SDE	RED-Diff	1000	8.53	0.050	38.89	0.951	7.27	0.090	36.88	0.892

D.1 Additional qualitative results

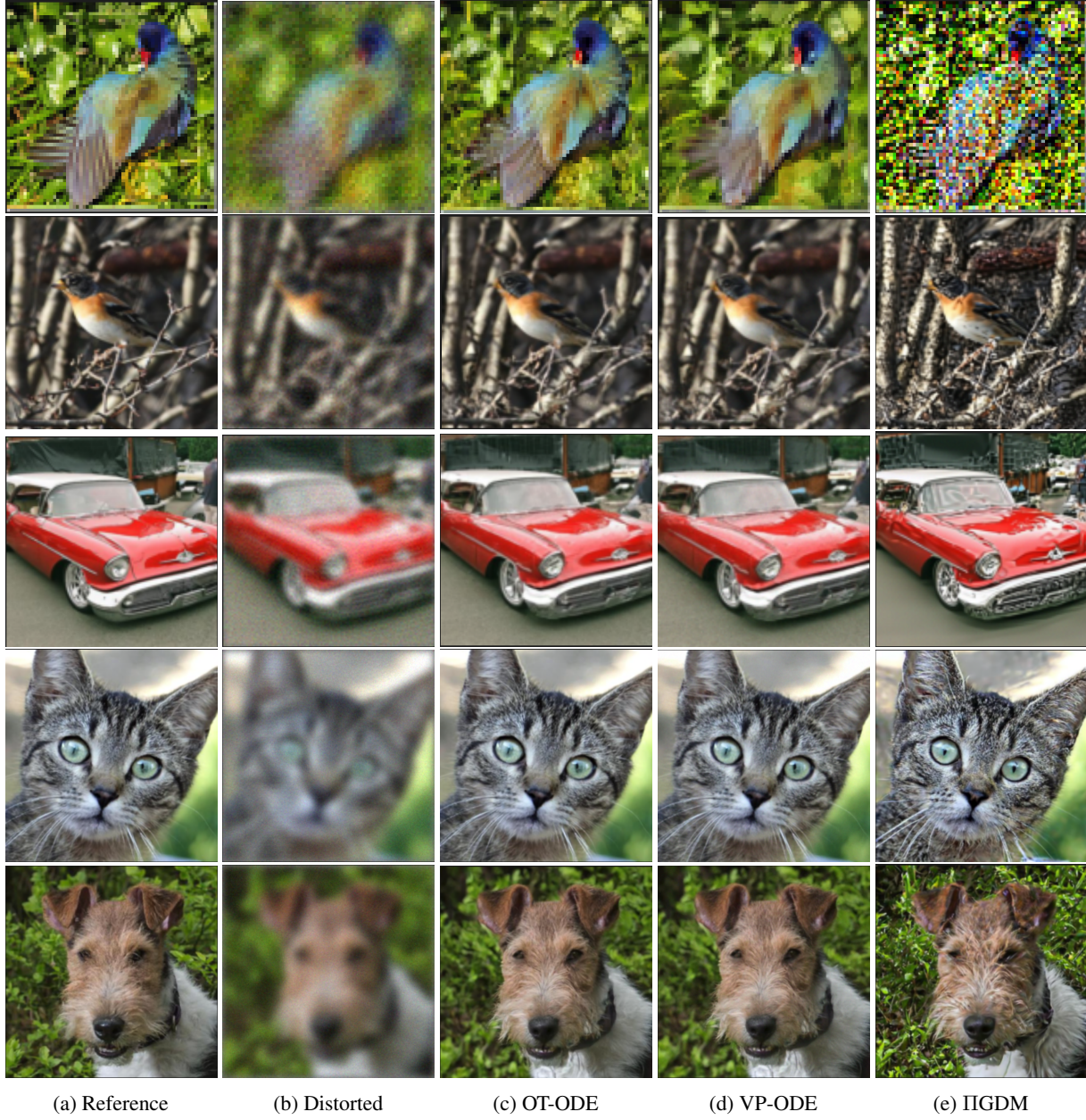


Figure 12: Gaussian-deblur with conditional OT model and $\sigma_y = 0.05$ for **(first row)** face-blurred ImageNet-64, **(second and third row)** face-blurred ImageNet-128, and **(fourth and fifth row)** AFHQ.

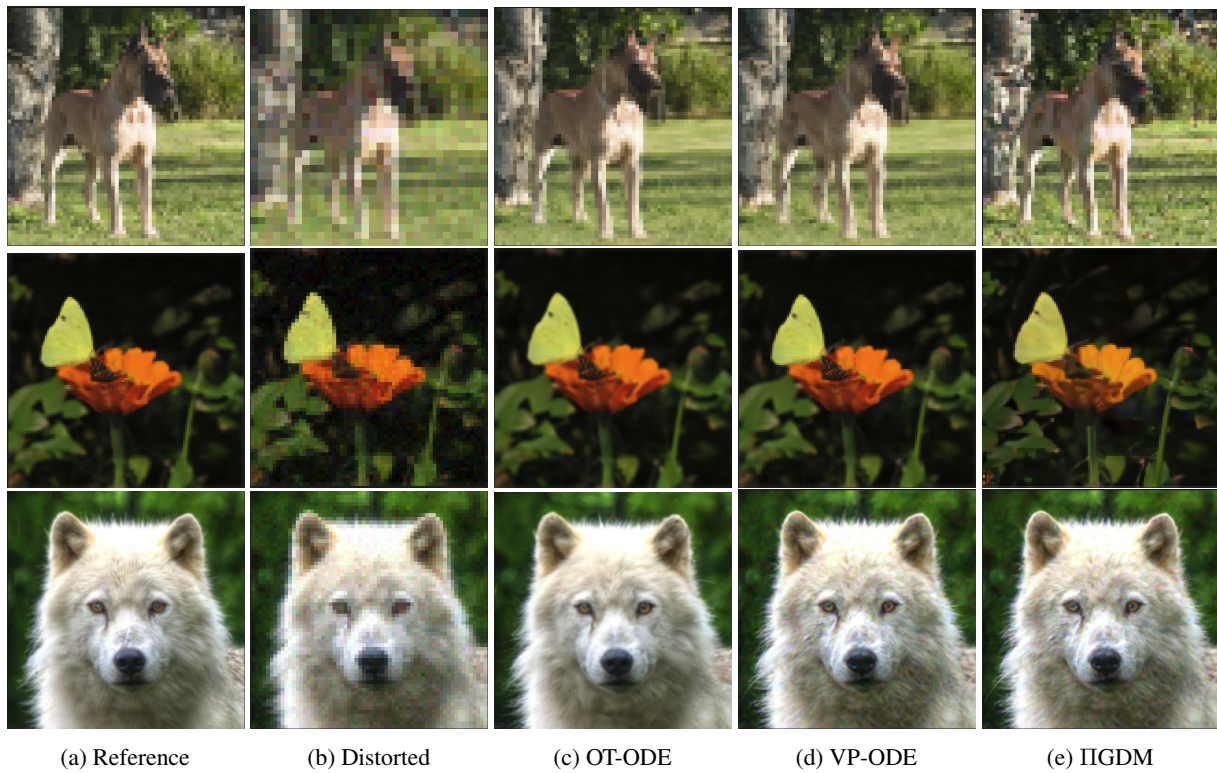


Figure 13: Super-resolution with conditional OT model and $\sigma_y = 0.05$ for **(first row)** face-blurred ImageNet-64 $2\times$, **(second row)** face-blurred ImageNet-128 $2\times$, and **(third row)** AFHQ $4\times$.

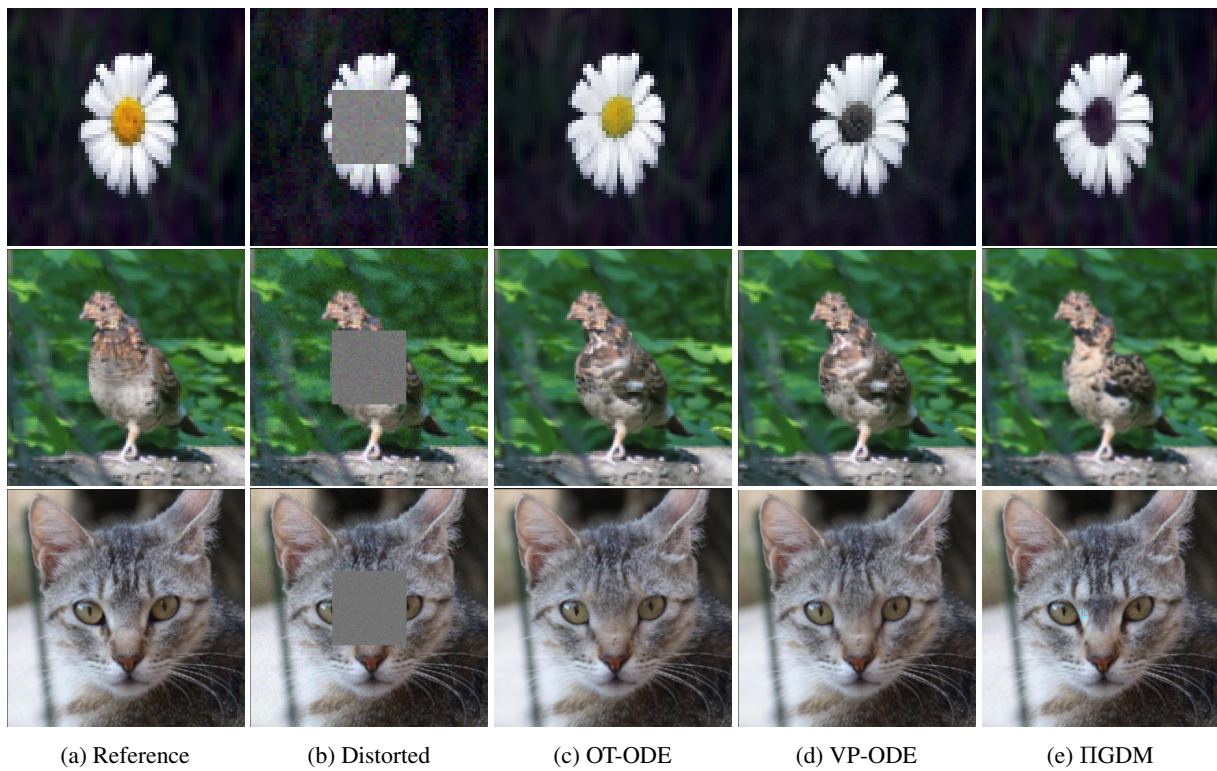


Figure 14: Inpainting (Center mask) with conditional OT model and $\sigma_y = 0.05$ for **(first row)** face-blurred ImageNet-64, **(second row)** face-blurred ImageNet-128, and **(third row)** AFHQ.



Figure 15: Inpainting (Free-form mask) with conditional OT model and $\sigma_y = 0.05$ for AFHQ.

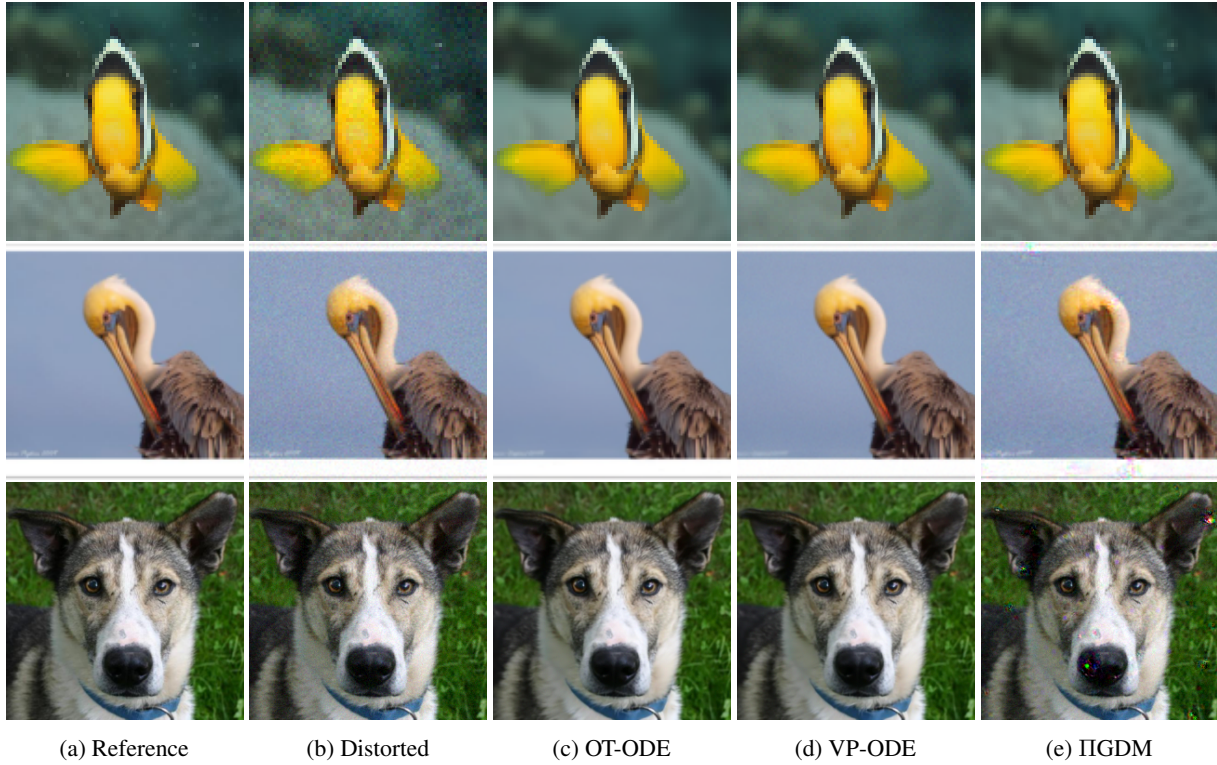


Figure 16: Denoising with conditional OT model and $\sigma_y = 0.05$ for **(first row)** face-blurred ImageNet-64, **(second row)** face-blurred ImageNet-128, and **(third row)** AFHQ.

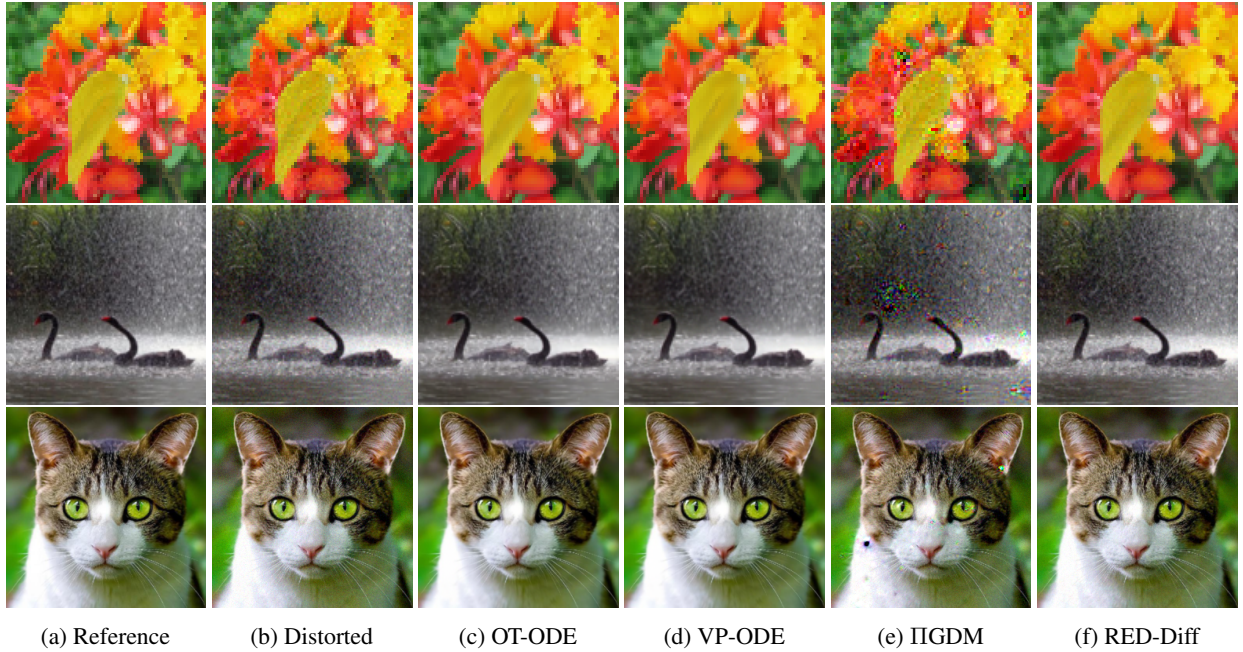


Figure 17: Denoising with pretrained VP-SDE model and $\sigma_y = 0.05$ for **(first row)** face-blurred ImageNet-64, **(second row)** face-blurred ImageNet-128, and **(third row)** AFHQ.

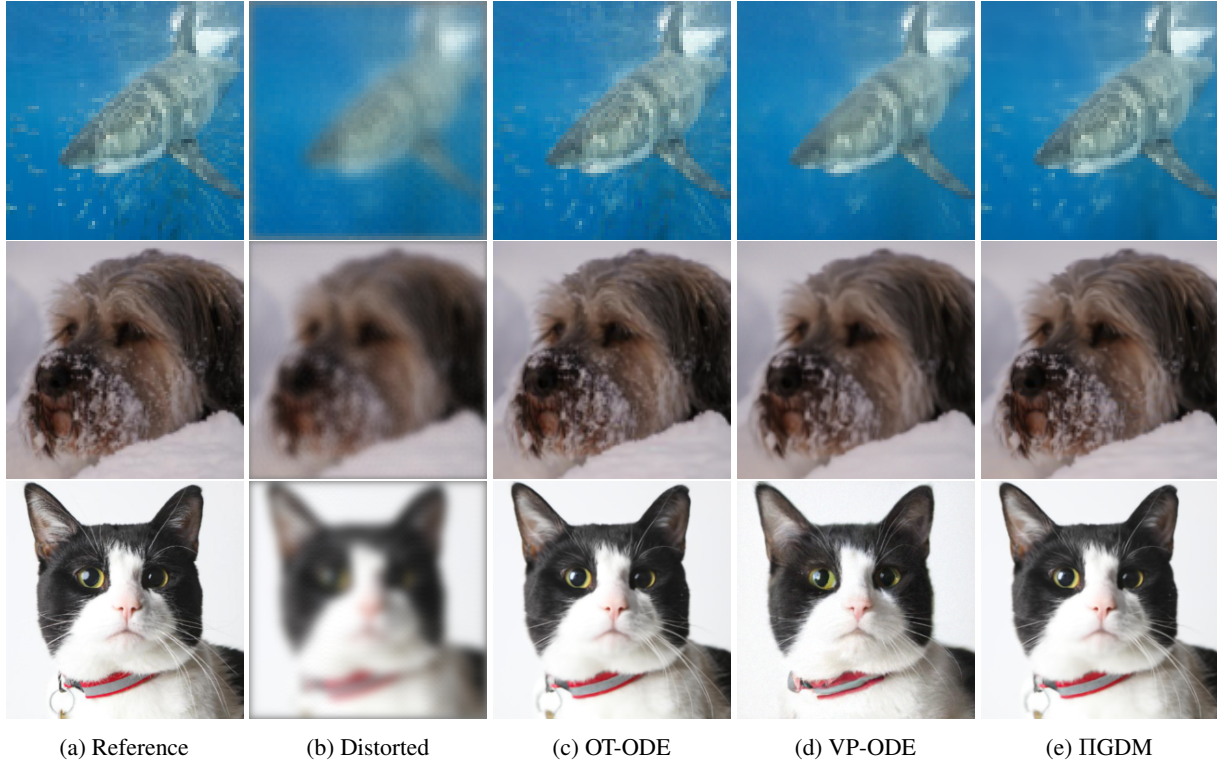


Figure 18: Gaussian deblurring with conditional OT model and $\sigma_y = 0$ for **(first row)** face-blurred ImageNet-64, **(second row)** face-blurred ImageNet-128 and **(third row)** AFHQ.



Figure 19: Super-resolution with conditional OT model and $\sigma_y = 0$ for **(first row)** face-blurred ImageNet-64, **(second row)** face-blurred ImageNet-128 and **(third row)** AFHQ.



Figure 20: Inpainting (centered mask) with conditional OT model and $\sigma_y = 0$ for **(first row)** face-blurred ImageNet-64, **(second row)** face-blurred ImageNet-128 and **(third row)** AFHQ.

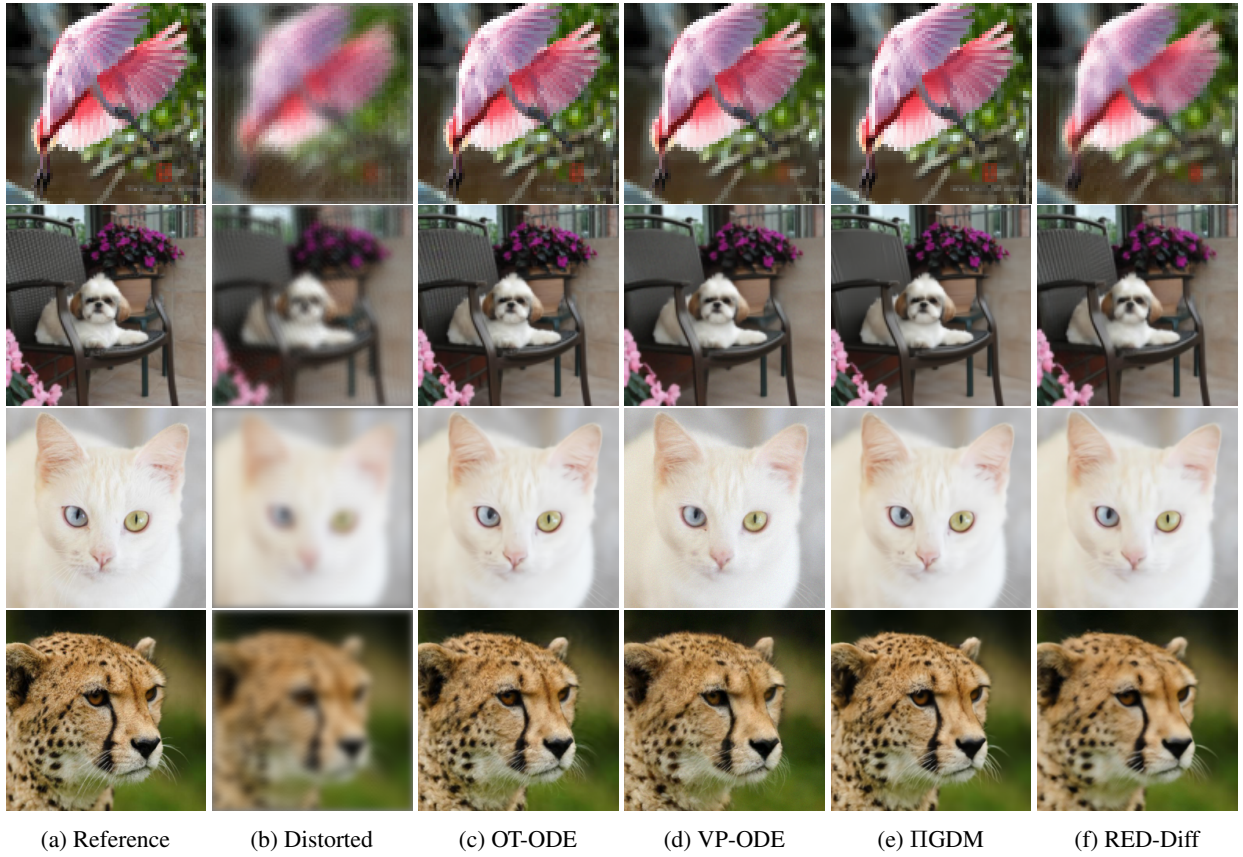


Figure 21: Gaussian deblurring with VP-SDE model and $\sigma_y = 0$ for **(first row)** face-blurred ImageNet-64, **(second row)** face-blurred ImageNet-128 and **(third and fourth row)** AFHQ.

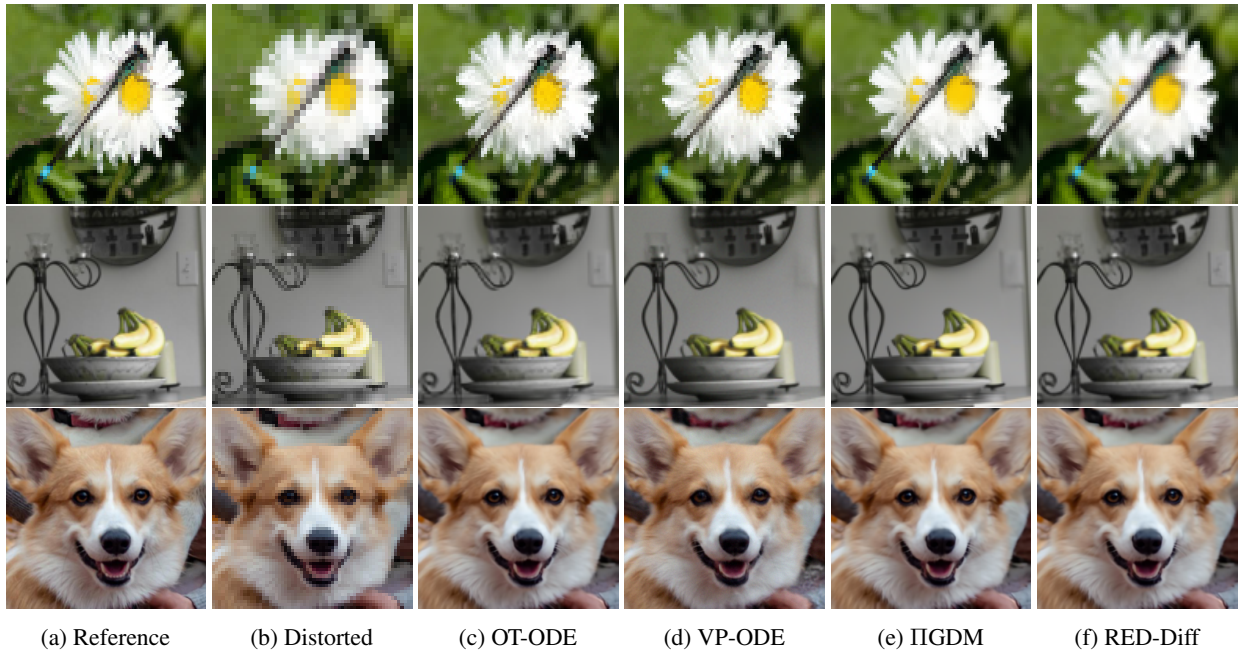


Figure 22: Super-resolution with VP-SDE model and $\sigma_y = 0$ for **(first row)** face-blurred ImageNet-64, **(second row)** face-blurred ImageNet-128 and **(third row)** AFHQ.

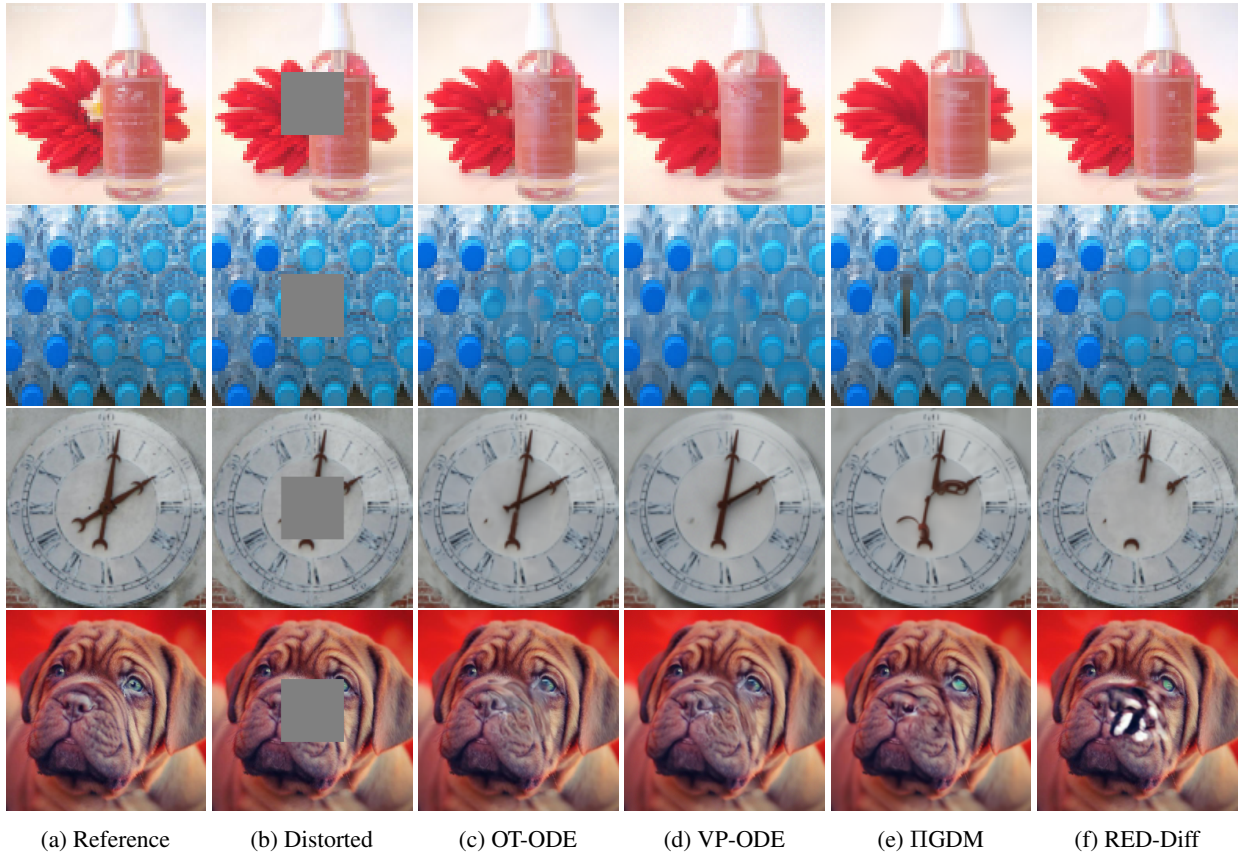


Figure 23: Inpainting (centered mask) with VP-SDE model and $\sigma_y = 0$ for **(first and second row)** face-blurred ImageNet-64, **(third row)** face-blurred ImageNet-128 and **(fourth row)** AFHQ.

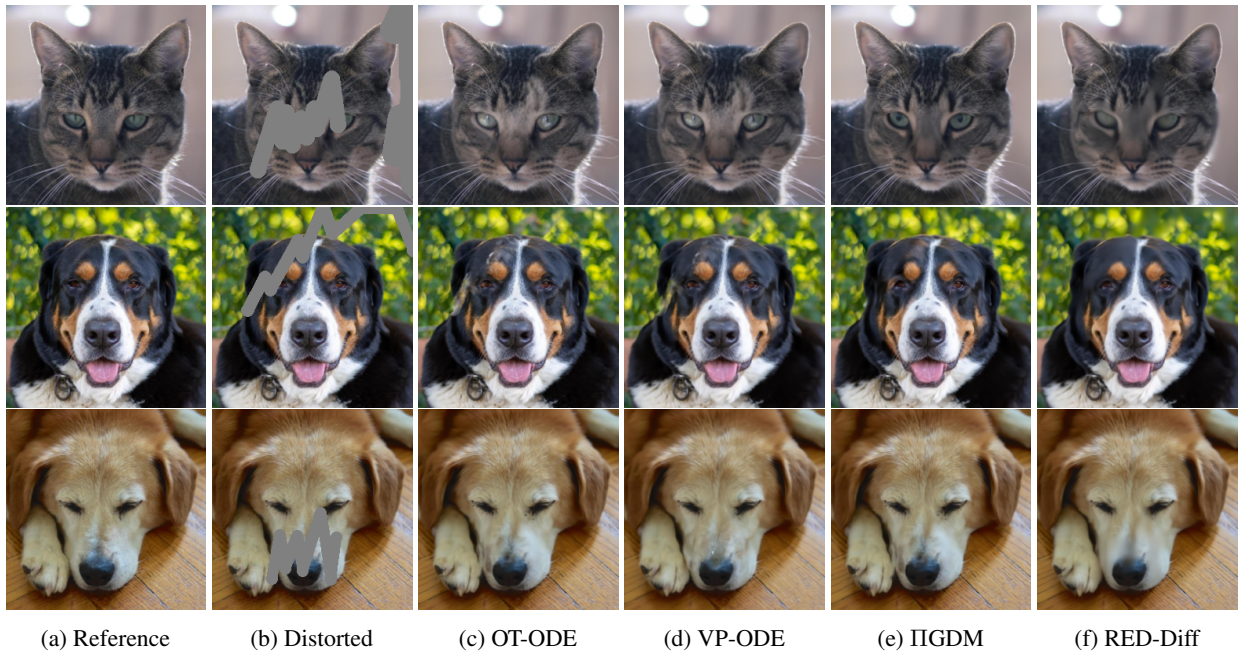


Figure 24: Inpainting (freeform mask) with VP-SDE model and $\sigma_y = 0$ for AFHQ.

D.2 Negative results from Inpainting



Figure 25: Negative results for inpainting with OT-ODE on AFHQ. We can observe artifacts in high-resolution images where the masked region is not inpainted correctly and there are patches in the inpainted region that are semantically incorrect. The observed artifacts are present in both the noiseless (e) and noisy (c) columns.

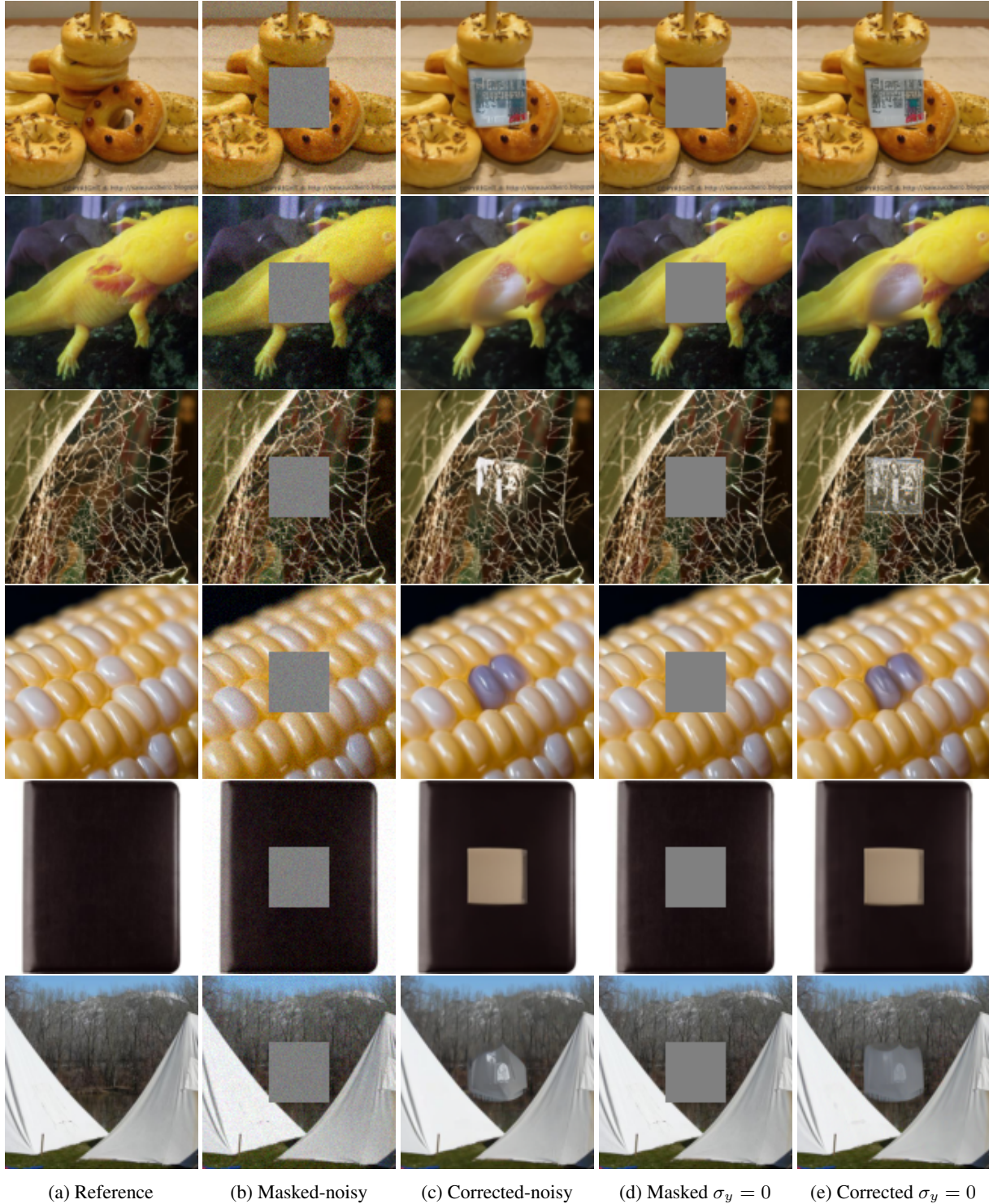


Figure 26: Negative results for inpainting with OT-ODE on face-blurred ImageNet-128. We can observe artifacts in high-resolution images where the masked region is not inpainted correctly and there are patches in the inpainted region that are semantically incorrect. The observed artifacts are present in both the noiseless (e) and noisy (c) columns.

E Noiseless null and range space decomposition

When $\sigma_y^2 = 0$, we can produce a vector field approximation with even lower Conditional Flow Matching loss by applying a null-space and range-space decomposition motivated by DDNM (Wang et al., 2022). In particular, when $\mathbf{y} = \mathbf{A}\mathbf{x}_1$, we have that $\mathbf{A}^\dagger \mathbf{y} = \mathbf{A}^\dagger \mathbf{A}\mathbf{x}_1$ (where \mathbf{A}^\dagger is the pseudo-inverse of \mathbf{A}) and so

$$\mathbb{E}_q[\mathbf{x}_1|\mathbf{x}_t, \mathbf{y}] = \mathbb{E}_q[\mathbf{A}^\dagger \mathbf{A}\mathbf{x}_1 + (\mathbf{I} - \mathbf{A}^\dagger \mathbf{A})\mathbf{x}_1|\mathbf{x}_t, \mathbf{y}] = \mathbf{A}^\dagger \mathbf{y} + (\mathbf{I} - \mathbf{A}^\dagger \mathbf{A})\mathbb{E}_q[\mathbf{x}_1|\mathbf{x}_t, \mathbf{y}]. \quad (18)$$

So when $\sigma_y^2 = 0$, it is only necessary to approximate the second term, as the first term is known through \mathbf{y} . The regression loss is minimized for the first term automatically and $\widehat{\mathbf{x}}_1(\mathbf{x}_t, \mathbf{y})$ is only responsible for predicting the second term.

In our experiments, we find that null space decomposition helps in inpainting but not other measurements. We summarize the results in Table 16 to 21 and show qualitative results for inpainting in Figure 27 to 29.

Table 16: Comparison of performance OT-ODE sampling and OT-ODE sampling with null and range space decomposition (NRSD) on face-blurred ImageNet-64 \times 64. For inpainting, OT-ODE sampling with null and range space decomposition outperforms simple OT-ODE sampling.

Model	Inference	NFEs \downarrow	Inpainting-Center, $\sigma_y = 0$			
			FID \downarrow	LPIPS \downarrow	PSNR \uparrow	SSIM \uparrow
OT	OT-ODE	80	4.94	0.080	37.42	0.885
OT	OT-ODE-NRSD	80	3.84	0.072	38.23	0.888
OT	VP-ODE	80	7.85	0.120	34.24	0.858
VP-SDE	OT-ODE	80	4.85	0.079	37.64	0.887
VP-SDE	OT-ODE-NRSD	80	3.77	0.072	38.24	0.888
VP-SDE	VP-ODE	80	7.21	0.117	34.33	0.860

Table 17: Comparison of performance OT-ODE sampling and OT-ODE sampling with null and range space decomposition (NRSD) on face-blurred ImageNet-64 \times 64. For tasks like super-resolution and Gaussian deblurring, OT-ODE sampling without null and range space decomposition outperforms other methods.

Model	Inference	NFEs \downarrow	SR 2 \times , $\sigma_y = 0$				Gaussian deblur, $\sigma_y = 0$			
			FID \downarrow	LPIPS \downarrow	PSNR \uparrow	SSIM \uparrow	FID \downarrow	LPIPS \downarrow	PSNR \uparrow	SSIM \uparrow
OT	OT-ODE	80	6.46	0.119	31.59	0.839	2.59	0.038	35.31	0.961
OT	OT-ODE-NRSD	80	7.37	0.134	31.05	0.799	3.05	0.044	35.19	0.956
OT	VP-ODE	80	8.29	0.147	31.20	0.817	6.13	0.083	33.31	0.929
VP-SDE	OT-ODE	80	6.32	0.118	31.60	0.839	2.61	0.037	35.45	0.963
VP-SDE	OT-ODE-NRSD	80	7.13	0.133	31.06	0.798	2.99	0.044	35.24	0.956
VP-SDE	VP-ODE	80	7.76	0.145	31.21	0.817	5.68	0.080	33.37	0.931

Table 18: Comparison of performance OT-ODE sampling and OT-ODE sampling with null and range space decomposition (NRSD) on face-blurred ImageNet-128 \times 128.

Model	Inference	NFEs \downarrow	SR 2 \times , $\sigma_y = 0$				Gaussian deblur, $\sigma_y = 0$			
			FID \downarrow	LPIPS \downarrow	PSNR \uparrow	SSIM \uparrow	FID \downarrow	LPIPS \downarrow	PSNR \uparrow	SSIM \uparrow
OT	OT-ODE	70	4.46	0.097	33.88	0.903	2.09	0.048	37.49	0.961
OT	OT-ODE-NRSD	70	3.62	0.099	33.24	0.876	1.42	0.036	38.35	0.969
OT	VP-ODE	70	7.69	0.144	32.93	0.871	6.02	0.108	34.73	0.925
VP-SDE	OT-ODE	70	4.62	0.096	33.95	0.906	2.26	0.046	37.79	0.967
VP-SDE	OT-ODE-NRSD	70	3.44	0.098	33.28	0.877	1.36	0.035	38.44	0.969
VP-SDE	VP-ODE	70	7.91	0.144	32.87	0.869	5.64	0.105	34.81	0.928

Table 19: Comparison of performance OT-ODE sampling and OT-ODE sampling with null and range space decomposition (NRSD) on face-blurred ImageNet-128 \times 128

Model	Inference	NFEs \downarrow	Inpainting- <i>Center</i> , $\sigma_y = 0$			
			FID \downarrow	LPIPS \downarrow	PSNR \uparrow	SSIM \uparrow
OT	OT-ODE	70	5.88	0.095	37.06	0.894
OT	OT-ODE-NRSD	70	3.95	0.074	38.27	0.906
OT	VP-ODE	70	8.63	0.144	34.48	0.864
VP-SDE	OT-ODE	70	5.93	0.094	37.31	0.898
VP-SDE	OT-ODE-NRSD	70	3.84	0.073	38.27	0.906
VP-SDE	VP-ODE	70	8.08	0.142	34.55	0.865

Table 20: Comparison of performance OT-ODE sampling and OT-ODE sampling with null and range space decomposition (NRSD) on AFHQ-256 \times 256

Model	Inference	NFEs \downarrow	SR 4 \times , $\sigma_y = 0$				Gaussian deblur, $\sigma_y = 0$			
			FID \downarrow	LPIPS \downarrow	PSNR \uparrow	SSIM \uparrow	FID \downarrow	LPIPS \downarrow	PSNR \uparrow	SSIM \uparrow
OT	OT-ODE	100	5.75	0.169	32.25	0.792	6.63	0.213	31.29	0.722
OT	OT-ODE-NRSD	100	5.73	0.179	31.69	0.753	7.32	0.237	30.72	0.665
OT	VP-ODE	100	6.14	0.194	31.93	0.773	7.38	0.231	31.10	0.705
VP-SDE	OT-ODE	100	6.58	0.178	32.18	0.789	8.24	0.226	31.21	0.717
VP-SDE	OT-ODE-NRSD	100	6.99	0.195	31.65	0.752	10.19	0.255	30.66	0.662
VP-SDE	VP-ODE	100	8.00	0.225	31.48	0.742	9.19	0.252	30.91	0.688

Table 21: Comparison of performance OT-ODE sampling and OT-ODE sampling with null and range space decomposition (NRSD) on AFHQ-256 \times 256

Model	Inference	NFEs \downarrow	Inpainting- <i>Center</i> , $\sigma_y = 0$				Inpainting- <i>Free-form</i> , $\sigma_y = 0$			
			FID \downarrow	LPIPS \downarrow	PSNR \uparrow	SSIM \uparrow	FID \downarrow	LPIPS \downarrow	PSNR \uparrow	SSIM \uparrow
OT	OT-ODE	100	8.87	0.061	37.45	0.921	4.98	0.097	36.15	0.889
OT	OT-ODE-NRSD	100	7.95	0.046	38.01	0.921	4.12	0.083	36.62	0.890
OT	VP-ODE	100	9.18	0.106	35.63	0.898	6.92	0.135	34.72	0.869
VP-SDE	OT-ODE	100	9.95	0.064	37.49	0.918	5.39	0.099	36.15	0.887
VP-SDE	OT-ODE-NRSD	100	10.96	0.052	37.95	0.916	4.87	0.089	36.52	0.884
VP-SDE	VP-ODE	100	10.50	0.112	35.59	0.893	7.36	0.139	34.65	0.865

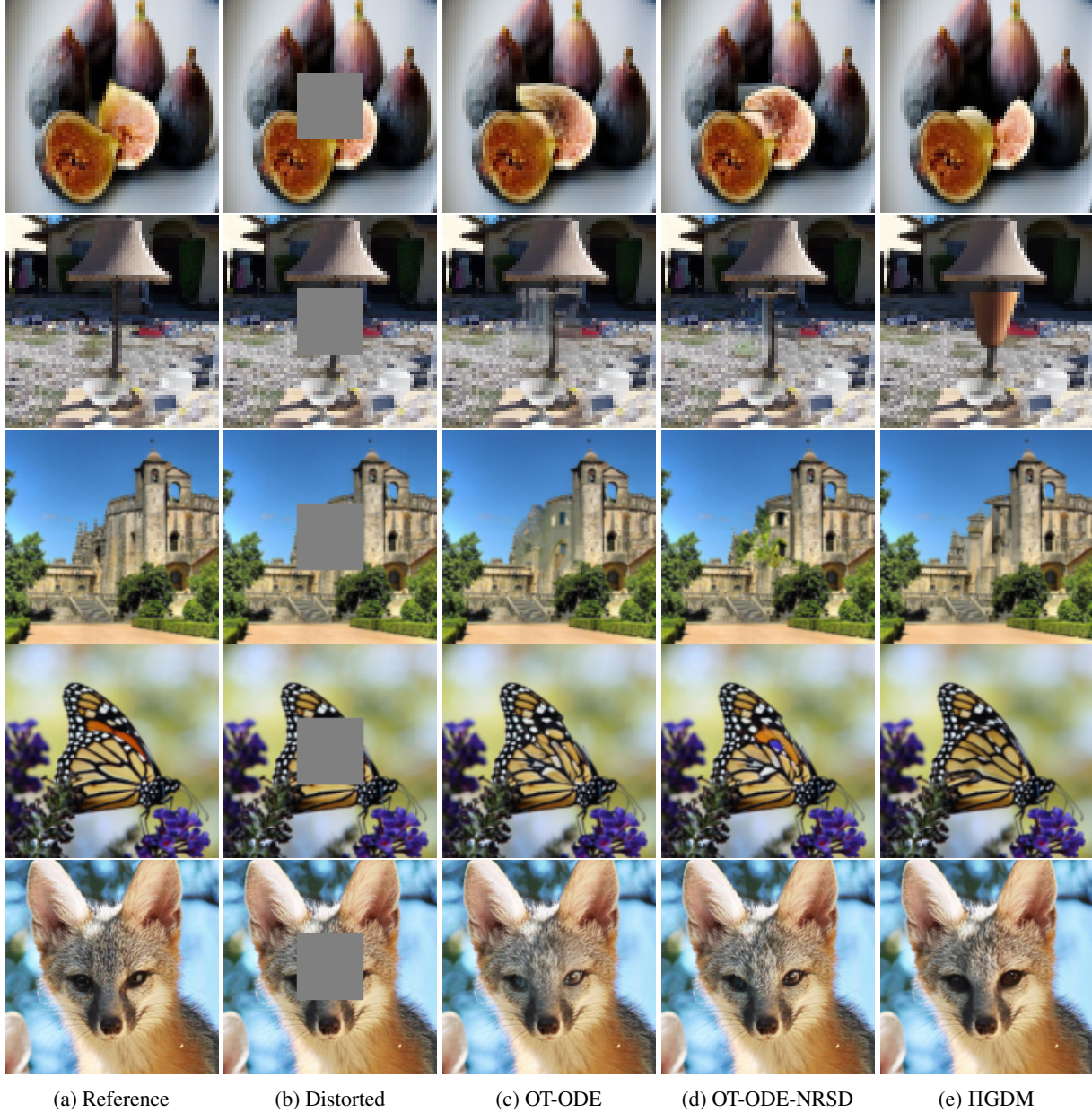


Figure 27: Comparison of inpainting (center mask) via OT-ODE sampling with and without null and range space decomposition (NRSD). We use conditional OT model and $\sigma_y = 0$ for **(first and second row)** face-blurred ImageNet-64, **(third row)** face-blurred ImageNet-128, and **(fourth row)** AFHQ.

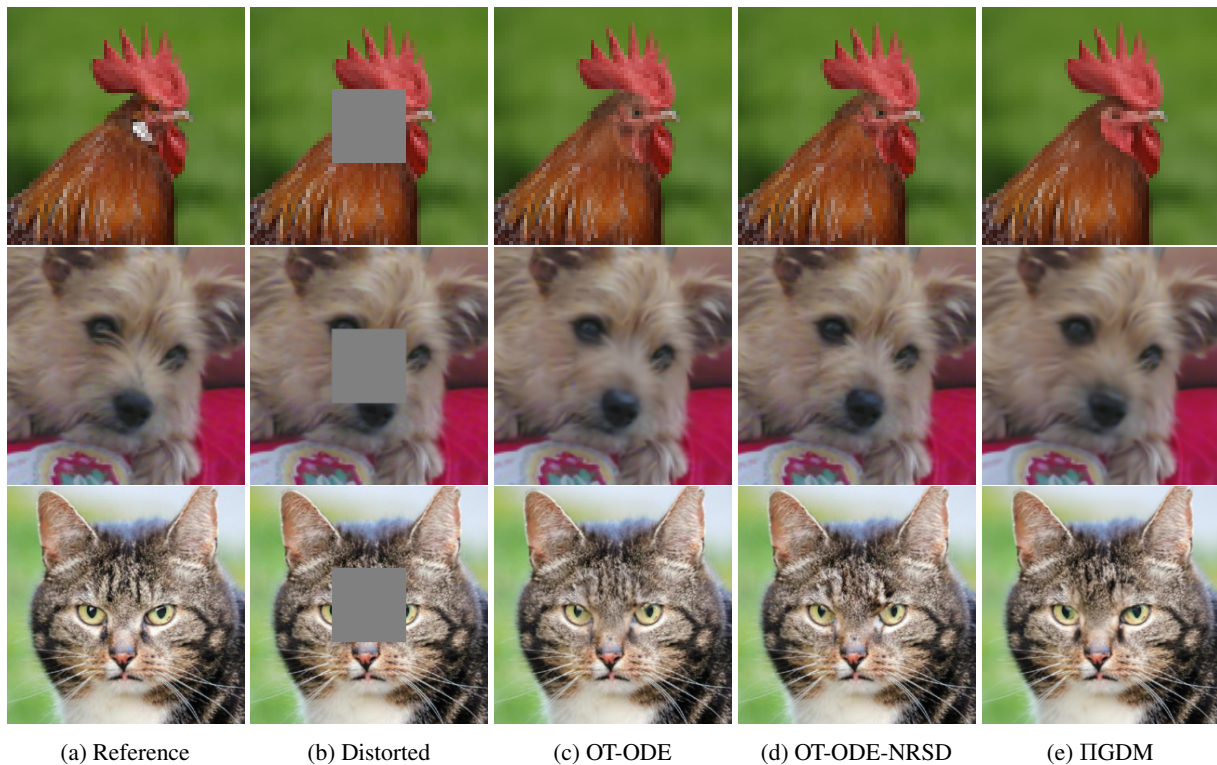


Figure 28: Comparison of inpainting (center mask) via OT-ODE sampling with and without null and range space decomposition (NRSD) for **(first row)** face-blurred ImageNet-64, **(second row)** face-blurred ImageNet-128, and **(third row)** AFHQ. We use VP-SDE model and $\sigma_y = 0$.

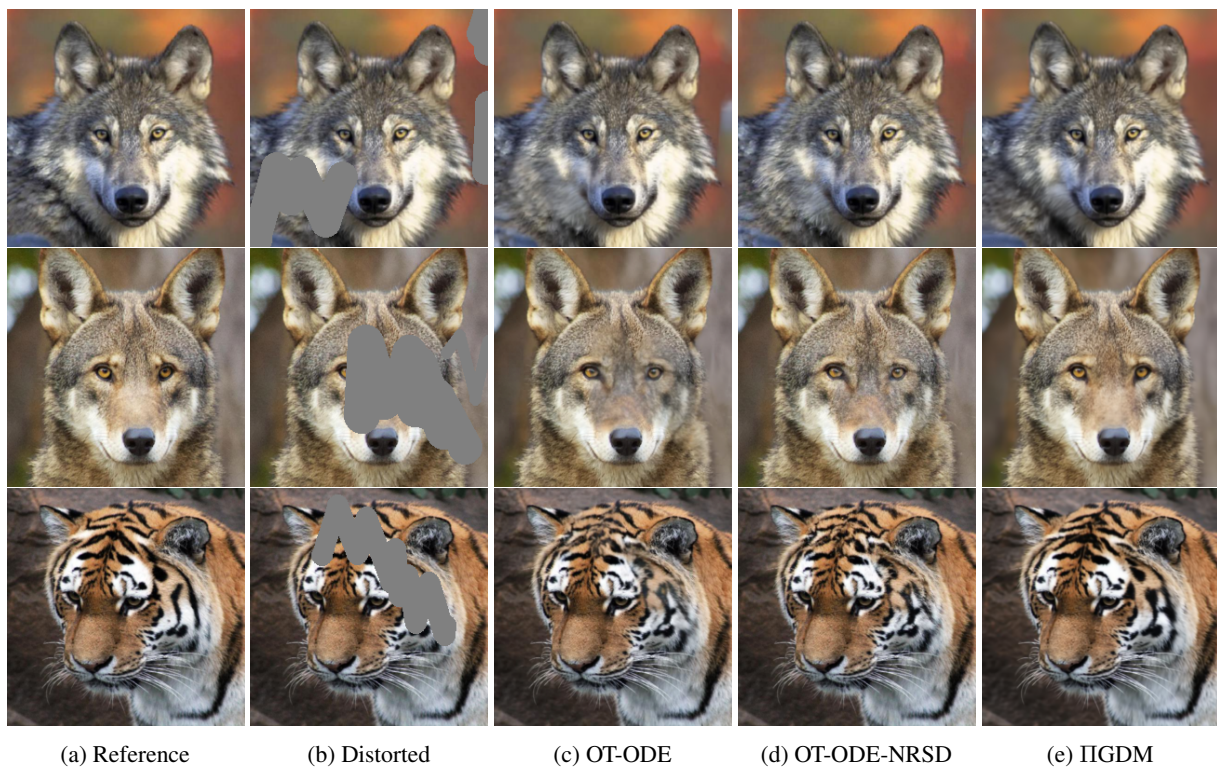


Figure 29: Comparison of inpainting (free-form mask) via OT-ODE sampling with and without null and range space decomposition (NRSD) for AFHQ. We use conditional OT model and $\sigma_y = 0$.

F Baselines

F.1 IIGDM

Implementation details. We closely follow the official code available on github while implementing IIGDM. For noisy case, we closely follow the Algorithm 1 in the appendix of Song et al. (2022). We use adaptive weighted guidance for both noiseless and noisy cases as in the original work. We always use uniform spacing while iterating the timestep over 100 steps. We use ascending time from 0 to 1. Note that the original paper uses descending time from T to 0. According to the notational convention used in this paper, this is equivalent to ascending time from 0 to 1. For the choice of r_t^2 , we consider the values derived from both variance exploding formulation and variance preserving formulation.

Value of r_t^2 . IIGDM sets the value of $r_t^2 = \frac{\sigma_{1-t}^2}{1+\sigma_{1-t}^2}$ for VE-SDE, where $q(\mathbf{x}_t|\mathbf{x}_1) = \mathcal{N}(\mathbf{x}_1, \sigma_{1-t}^2 \mathbf{I})$. We can follow the same procedure as outlined in Song et al. (2022), and solve for r_t^2 in closed form for VP-SDE. We know for that VP-SDE, $q(\mathbf{x}_t|\mathbf{x}_1) = \mathcal{N}(\alpha_{1-t}\mathbf{x}_1, (1 - \alpha_{1-t}^2)\mathbf{I})$, where $\alpha_t = e^{-\frac{1}{2}T(t)}$, $T(t) = \int_0^t \beta(s)ds$, and $\beta(s)$ is the noise scale function. Using equation 13 for VP-SDE gives $r_t^2 = 1 - \alpha_{1-t}^2$. We can also obtain an alternate r_t^2 by plugging in value of σ_t^2 for VP-SDE into the expression of r_t^2 derived for VE-SDE, which evaluates to $r_t^2 = \frac{1-\alpha_{1-t}^2}{2-\alpha_{1-t}^2}$. Empirically, we find that r_t^2 for VE-SDE marginally outperforms VP-SDE. We report performance of IIGDM with both choices of r_t^2 in Table 22 to 24.

Table 22: Relative performance of IIGDM on face-blurred ImageNet-64 with VE and VP derived r_t^2 with $\sigma_y = 0.05$

Measurement	Model	VP				VE			
		FID ↓	LPIPS ↓	PSNR ↑	SSIM ↑	FID ↓	LPIPS ↓	PSNR ↑	SSIM ↑
SR 2×	OT	6.52	0.168	30.54	0.753	5.91	0.160	30.60	0.762
Gaussian deblur	OT	55.19	0.374	28.74	0.516	39.36	0.326	29.00	0.572
Inpainting-Center	OT	9.25	0.111	34.13	0.863	8.70	0.109	34.17	0.864
Denoising	OT	16.59	0.102	34.60	0.906	16.44	0.101	34.64	0.907
SR 2×	VP-SDE	6.84	0.174	30.48	0.743	6.11	0.166	30.54	0.753
Gaussian deblur	VP-SDE	54.77	0.376	28.74	0.511	39.14	0.329	28.99	0.567
Inpainting-Center	VP-SDE	9.75	0.113	34.03	0.860	9.36	0.112	34.06	0.862
Denoising	VP-SDE	17.19	0.107	34.25	0.901	15.54	0.102	34.41	0.906

Table 23: Relative performance of IIGDM on face-blurred ImageNet-128 with VE and VP derived r_t^2 with $\sigma_y = 0.05$

Measurement	Model	VP				VE			
		FID ↓	LPIPS ↓	PSNR ↑	SSIM ↑	FID ↓	LPIPS ↓	PSNR ↑	SSIM ↑
SR 2×	OT	4.38	0.148	32.07	0.831	4.26	0.145	32.12	0.834
Gaussian deblur	OT	30.30	0.328	29.96	0.606	22.42	0.296	30.17	0.642
Inpainting-Center	OT	7.99	0.122	34.57	0.867	7.64	0.120	34.61	0.869
Denoising	OT	9.60	0.107	35.11	0.903	9.30	0.104	35.21	0.906
SR 2×	VP-SDE	7.55	0.183	31.61	0.785	6.14	0.168	31.79	0.803
Gaussian deblur	VP-SDE	55.61	0.463	28.57	0.414	41.69	0.404	28.98	0.493
Inpainting-Center	VP-SDE	9.75	0.130	34.45	0.858	9.46	0.129	34.49	0.859
Denoising	VP-SDE	10.69	0.124	34.72	0.882	10.11	0.119	34.92	0.886

Choice of starting time. For OT-ODE sampling and VP-ODE sampling, we observe that starting at time $t > 0$ improves the performance. We therefore perform an ablation study on IIGDM baseline, and vary the start time to verify whether starting at $t > 0$ helps to improve the performance. We plot the metrics for three different measurements in Figure 30. We observe that starting later at time $t > 0$ consistently leads to worse performance compared to starting at time $t = 0$. Therefore, for all our experiments with IIGDM, we always start at time $t = 0$.

Table 24: Relative performance of IIGDM on AFHQ with VE and VP derived r_t^2 with $\sigma_y = 0.05$

Measurement	Model	VP				VE			
		FID ↓	LPIPS ↓	PSNR ↑	SSIM ↑	FID ↓	LPIPS ↓	PSNR ↑	SSIM ↑
SR 4×	OT	12.69	0.285	30.18	0.665	12.31	0.282	30.23	0.672
Gaussian deblur	OT	24.60	0.383	28.93	0.429	19.66	0.355	29.16	0.475
Inpainting-Center	OT	19.09	0.153	34.20	0.855	16.51	0.145	34.40	0.863
Denoising	OT	11.20	0.159	34.49	0.876	10.92	0.153	34.78	0.883
SR 4×	VP-SDE	77.49	0.469	29.34	0.469	54.12	0.413	29.73	0.549
Gaussian deblur	VP-SDE	116.42	0.535	28.49	0.313	95.09	0.493	28.74	0.368
Inpainting-Center	VP-SDE	57.46	0.239	32.40	0.773	56.86	0.238	32.42	0.775
Denoising	VP-SDE	81.15	0.451	29.62	0.639	35.33	0.278	31.72	0.776

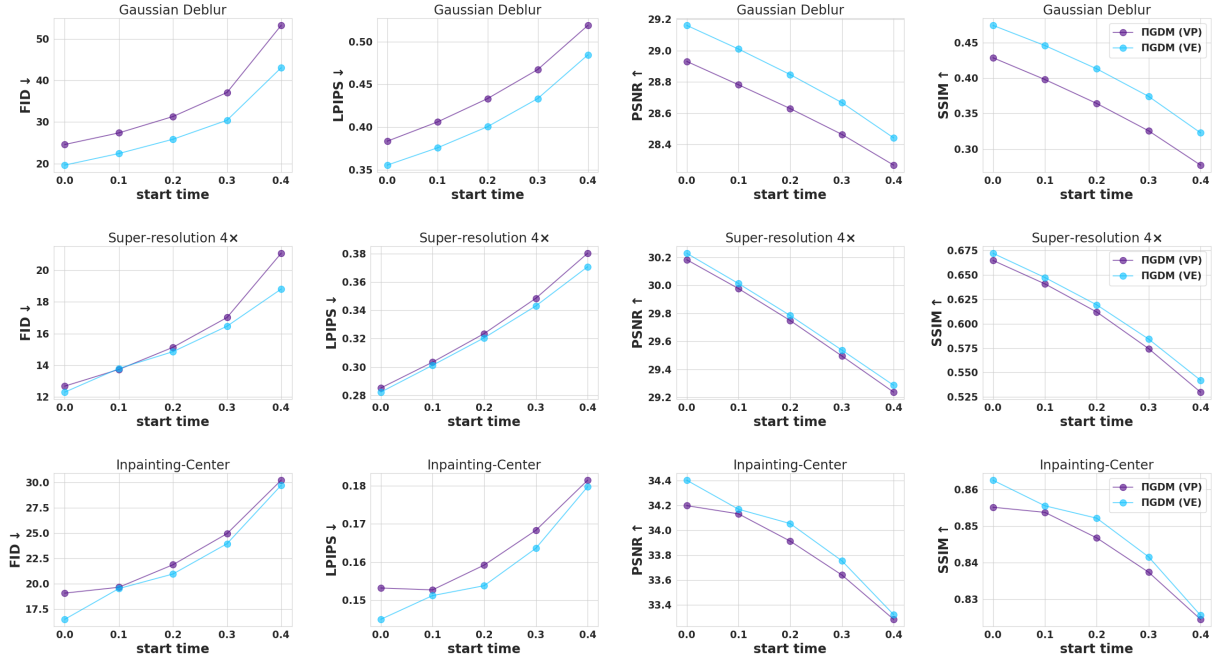


Figure 30: Variation in performance IIGDM sampling with variation in start times on AFHQ dataset. We use pretrained conditional OT model and set $\sigma_y = 0.05$. We observe similar trends with VP-SDE checkpoint. We plot metrics for both choices of r_t^2 that can be derived from variance preserving and variance exploding formulations.

F.2 RED-Diff

Implementation details. We use VP-SDE model for all experiments with RED-Diff. We closely follow the official code available on github while implementing RED-Diff. Similar to (Mardani et al., 2023), we always use uniform spacing while iterating the timestep over 1000 steps. We use ascending time from 0 to 1. Note that the original paper uses descending time from T to 0. According to the notational convention used in this paper, this is equivalent to ascending time from 0 to 1. We use Adam optimizer and use the momentum pair (0.9, 0.99) similar to the original work. Further, we use initial learning rate of 0.1 for AFHQ and ImageNet-128, as used in the original work, and learning rate of 0.01 for ImageNet-64. We use batch size of 1 for all the experiments. Finally, we extensively tuned the regularization hyperparameter λ to find the value that results in optimal performance across all metrics. We summarize the results of our experiments in Table 25 to 30. We note that more extensive tuning may be able to find better performing hyperparameters but this goes against the intent of a training-free algorithm.

Table 25: Hyperparameter search for RED-Diff on face-blurred ImageNet- 64×64 with $\sigma_y = 0.05$. We use learning rate of 0.01.

λ	SR $2\times$, $\sigma_y = 0.05$				Gaussian deblur, $\sigma_y = 0.05$			
	FID \downarrow	LPIPS \downarrow	PSNR \uparrow	SSIM \uparrow	FID \downarrow	LPIPS \downarrow	PSNR \uparrow	SSIM \uparrow
0.1	34.09	0.224	30.12	0.798	46.76	0.254	29.29	0.715
0.25	28.45	0.206	30.40	0.814	51.20	0.236	30.19	0.776
0.75	23.02	0.187	31.22	0.839	73.76	0.287	30.47	0.750
1.5	32.35	0.243	30.80	0.792	82.26	0.335	30.29	0.705
2.0	40.33	0.284	30.41	0.750	86.48	0.358	30.17	0.683

λ	Inpainting-Center, $\sigma_y = 0.05$				Denoising, $\sigma_y = 0.05$			
	FID \downarrow	LPIPS \downarrow	PSNR \uparrow	SSIM \uparrow	FID \downarrow	LPIPS \downarrow	PSNR \uparrow	SSIM \uparrow
0.1	15.71	0.155	31.74	0.840	12.47	0.085	32.24	0.907
0.25	15.56	0.155	31.73	0.839	11.80	0.083	32.36	0.908
0.75	13.31	0.139	32.65	0.857	8.43	0.062	33.65	0.932
1.5	12.18	0.119	33.97	0.881	6.11	0.041	35.34	0.958
2.0	12.87	0.119	34.19	0.886	6.02	0.041	35.64	0.964

Table 26: Hyperparameter search for RED-Diff on face-blurred ImageNet- 64×64 with $\sigma_y = 0$. We use learning rate of 0.01.

λ	SR $2\times$, $\sigma_y = 0$				Gaussian deblur, $\sigma_y = 0$			
	FID \downarrow	LPIPS \downarrow	PSNR \uparrow	SSIM \uparrow	FID \downarrow	LPIPS \downarrow	PSNR \uparrow	SSIM \uparrow
0.1	11.74	0.224	30.12	0.798	15.39	0.134	31.99	0.879
0.25	12.65	0.130	32.34	0.886	29.56	0.236	30.19	0.776
0.75	20.36	0.187	31.22	0.839	55.43	0.287	30.47	0.750
1.5	33.13	0.243	30.80	0.792	71.64	0.335	30.29	0.705
2.0	41.56	0.288	30.46	0.752	78.55	0.358	30.22	0.685

Inpainting-Center, $\sigma_y = 0$				
λ	FID \downarrow	LPIPS \downarrow	PSNR \uparrow	SSIM \uparrow
0.1	7.29	0.079	39.14	0.925
0.25	7.40	0.155	31.73	0.839
0.75	8.47	0.083	38.59	0.922
1.5	10.75	0.095	37.42	0.916
2.0	12.54	0.119	34.19	0.886

Table 27: Hyperparameter search for RED-Diff on face-blurred ImageNet- 128×128 with $\sigma_y = 0.05$. We use learning rate of 0.1.

λ	SR $2\times$, $\sigma_y = 0.05$				Gaussian deblur, $\sigma_y = 0.05$			
	FID \downarrow	LPIPS \downarrow	PSNR \uparrow	SSIM \uparrow	FID \downarrow	LPIPS \downarrow	PSNR \uparrow	SSIM \uparrow
0.1	23.25	0.272	30.12	0.731	37.83	0.42	28.54	0.473
0.75	14.56	0.224	30.71	0.782	21.43	0.229	31.41	0.807
1.5	10.54	0.182	31.82	0.852	22.85	0.247	31.65	0.809
2.0	11.65	0.187	31.93	0.859	24.71	0.259	31.61	0.802

λ	Inpainting-Center, $\sigma_y = 0.05$				Denoising, $\sigma_y = 0.05$			
	FID \downarrow	LPIPS \downarrow	PSNR \uparrow	SSIM \uparrow	FID \downarrow	LPIPS \downarrow	PSNR \uparrow	SSIM \uparrow
0.1	19.68	0.191	31.75	0.795	12.83	0.134	32.27	0.854
0.75	19.03	0.202	31.36	0.779	12.69	0.14	32.09	0.846
1.5	16.33	0.189	31.81	0.794	10.67	0.121	32.89	0.874
2.0	14.63	0.171	32.42	0.819	9.19	0.105	33.52	0.895

Table 28: Hyperparameter search for RED-Diff on face-blurred ImageNet- 128×128 with $\sigma_y = 0$. We use learning rate of 0.1.

λ	SR $2\times$, $\sigma_y = 0$				Gaussian deblur, $\sigma_y = 0$			
	FID \downarrow	LPIPS \downarrow	PSNR \uparrow	SSIM \uparrow	FID \downarrow	LPIPS \downarrow	PSNR \uparrow	SSIM \uparrow
0.1	3.90	0.082	34.47	0.922	4.19	0.085	34.68	0.929
0.75	6.52	0.105	33.54	0.905	12.59	0.177	32.71	0.864
1.5	10.46	0.142	32.98	0.894	19.29	0.225	32.15	0.831
2.0	13.08	0.165	32.65	0.884	22.57	0.245	31.94	0.816

λ	Inpainting-Center, $\sigma_y = 0$				Inpainting-Freeform, $\sigma_y = 0$			
	FID \downarrow	LPIPS \downarrow	PSNR \uparrow	SSIM \uparrow	FID \downarrow	LPIPS \downarrow	PSNR \uparrow	SSIM \uparrow
0.1	5.39	0.068	38.91	0.928	8.94	0.162	35.54	0.830
0.75	5.52	0.073	38.11	0.924	9.26	0.166	35.05	0.826
1.5	6.09	0.079	37.32	0.920	10.13	0.172	34.58	0.821
2.0	6.68	0.083	36.87	0.917	10.87	0.176	34.30	0.818

Table 29: Hyperparameter search for RED-Diff on AFHQ with $\sigma_y = 0.5$. We use learning rate of 0.1.

λ	SR 4 \times , $\sigma_y = 0.05$				Gaussian deblur, $\sigma_y = 0.05$			
	FID \downarrow	LPIPS \downarrow	PSNR \uparrow	SSIM \uparrow	FID \downarrow	LPIPS \downarrow	PSNR \uparrow	SSIM \uparrow
0.1	21.59	0.385	29.51	0.607	17.36	0.379	29.95	0.639
0.25	22.47	0.374	29.66	0.635	15.81	0.341	30.15	0.645
0.75	20.84	0.331	29.97	0.675	25.41	0.366	29.76	0.588
1.5	22.46	0.355	29.68	0.642	38.66	0.409	29.34	0.525
2.0	25.02	0.376	29.49	0.618	45.01	0.427	29.18	0.500

λ	Inpainting-Center, $\sigma_y = 0.05$				Denoising, $\sigma_y = 0.05$			
	FID \downarrow	LPIPS \downarrow	PSNR \uparrow	SSIM \uparrow	FID \downarrow	LPIPS \downarrow	PSNR \uparrow	SSIM \uparrow
0.1	28.39	0.216	31.53	0.756	8.32	0.159	32.18	0.827
0.25	28.85	0.217	31.51	0.755	8.35	0.161	32.16	0.826
0.75	28.80	0.218	31.64	0.759	7.94	0.156	32.35	0.833
1.5	28.74	0.205	32.19	0.784	6.63	0.138	33.12	0.862
2.0	28.55	0.190	32.63	0.802	5.71	0.124	33.70	0.882
2.5	28.71	0.177	32.99	0.818	4.93	0.111	34.18	0.899

Table 30: Hyperparameter search for RED-Diff on AFHQ with $\sigma_y = 0$. We use learning rate (lr) of 0.1 unless mentioned otherwise.

λ	SR 4 \times , $\sigma_y = 0$				Gaussian deblur, $\sigma_y = 0$			
	FID \downarrow	LPIPS \downarrow	PSNR \uparrow	SSIM \uparrow	FID \downarrow	LPIPS \downarrow	PSNR \uparrow	SSIM \uparrow
0.005	11.67	0.197	32.93	0.837	14.69	0.278	31.73	0.760
0.05	8.65	0.191	32.21	0.801	11.67	0.268	31.30	0.731
0.1	9.65	0.204	31.84	0.781	11.53	0.273	31.05	0.711
0.25	11.65	0.222	31.53	0.768	13.22	0.293	30.63	0.675
0.75	14.98	0.274	30.72	0.726	23.34	0.351	29.91	0.598
1.5	19.40	0.332	29.95	0.665	36.96	0.402	29.39	0.529
2.0	22.72	0.361	29.65	0.632	43.64	0.422	29.22	0.504

λ	Inpainting-Center, $\sigma_y = 0$, lr=0.01				Inpainting-Freeform, $\sigma_y = 0$			
	FID \downarrow	LPIPS \downarrow	PSNR \uparrow	SSIM \uparrow	FID \downarrow	LPIPS \downarrow	PSNR \uparrow	SSIM \uparrow
0.005	8.53	0.050	38.89	0.951	7.22	0.091	36.89	0.892
0.05	8.53	0.050	38.89	0.951	7.27	0.090	36.88	0.892
0.1	8.53	0.050	38.88	0.951	7.23	0.091	36.82	0.891
0.25	8.53	0.050	38.83	0.950	7.32	0.094	36.69	0.889
0.75	8.88	0.056	38.60	0.948	7.74	0.102	36.26	0.884
1.5	10.32	0.071	38.04	0.942	8.41	0.112	35.69	0.877
2.0	11.62	0.084	37.54	0.937	8.76	0.119	35.37	0.872

G Additional Background

In this section, we follow the notation used in the prior work by [Lipman et al. \(2022\)](#).

Continuous Normalizing Flows (CNFs). A Continuous Normalizing Flow ([Chen et al., 2018a](#)) is a time-dependent diffeomorphic map $\phi_t : [0, 1] \times \mathbb{R}^d \rightarrow \mathbb{R}^d$ that is defined by the ODE:

$$\frac{d}{dt}\phi_t(\mathbf{x}) = \mathbf{v}_t(\phi_t(\mathbf{x})); \quad \phi_0(\mathbf{x}) = \mathbf{x} \quad (19)$$

where $\mathbf{x} \in \mathbb{R}^d$ and $\mathbf{v}_t : [0, 1] \times \mathbb{R}^d \rightarrow \mathbb{R}^d$ is a time-dependent vector field that is usually parametrized with a neural network. The generative process of a CNF involves sampling from a simple prior distribution $\mathbf{x}_0 \sim p_0(\mathbf{x}_0)$ (e.g. standard Gaussian distribution) and then solving the initial value problem defined by the ODE in Eq. (19) to obtain a sample from the target distribution $\mathbf{x}_1 \sim p_1(\mathbf{x}_1)$. Thus, a CNF reshapes a simple prior distribution p_0 to a more complex distribution p_t , via a push-forward equation based on the instantaneous change of variables formula.

$$p_t = [\phi]_* p_0 \quad (20)$$

$$[\phi]_* p_0(\mathbf{x}) = p_0(\phi_t^{-1}(\mathbf{x})) \det \left[\frac{\partial \phi_t^{-1}}{\partial \mathbf{x}}(\mathbf{x}) \right] \quad (21)$$

CNFs are usually trained by optimizing the maximum likelihood objective. As shown in [Chen et al. \(2018a\)](#), the exact likelihood computation can be done via relatively cheap operations despite the Jacobian term. However, this requires restricting the architecture of the neural network to constrain the Jacobian term. FFJORD ([Grathwohl et al., 2018](#)) improves upon this by proposing a method that uses Hutchinson’s trace estimator to compute log density, and allows CNFs with free-form Jacobians, thereby removing any restrictions on the architecture. This approach has difficulties for high-dimensional images where the trace estimator is noisy. Flow Matching provides an alternative, scalable approach to training CNFs with arbitrary architectures.

Flow Matching. Suppose we have samples from an unknown data distribution $\mathbf{x}_1 \sim q(\mathbf{x}_1)$. Let p_t denote a probability path from the prior distribution p_0 to the data distribution p_1 that is approximately equal to q . Flow Matching loss is defined as

$$\mathcal{L}_{FM} = \mathbb{E}_{t, p_t(\mathbf{x})} \|\mathbf{v}_t(\mathbf{x}; \theta) - \mathbf{u}_t(\mathbf{x})\|^2 \quad (22)$$

where $\mathbf{u}_t(\mathbf{x})$ is a vector field that generates the probability path $p_t(\mathbf{x})$, and θ denotes trainable parameters of the CNF. In practice, we usually do not have any prior knowledge on p_t and \mathbf{u}_t , and thus this objective is intractable. Inspired by diffusion models, [Lipman et al. \(2022\)](#) propose Conditional Flow Matching, where both the probability paths and the vector fields are conditioned on the sample $\mathbf{x}_1 \sim q(\mathbf{x}_1)$. The exact objective for Conditional Flow matching is given by

$$\mathcal{L}_{CFM} = \mathbb{E}_{t, q(\mathbf{x}_1), p_t(\mathbf{x}|\mathbf{x}_1)} \|\mathbf{v}_t(\mathbf{x}; \theta) - \mathbf{u}_t(\mathbf{x}|\mathbf{x}_1)\|^2 \quad (23)$$

where, $p_t(\mathbf{x}|\mathbf{x}_1)$ denotes a conditional probability path, and $\mathbf{u}_t(\mathbf{x}|\mathbf{x}_1)$ denotes the corresponding conditional vector field that generates the conditional probability path. Interestingly, both the loss objectives in Eq. (23) and Eq. (22) have identical gradients w.r.t. θ . More importantly, past research has proven that $\mathbf{u}_t(\mathbf{x}) = \mathbb{E}[\mathbf{u}_t(\mathbf{x}|\mathbf{x}_1)|\mathbf{x}_t = \mathbf{x}]$. The optimal solution to the conditional Flow Matching recovers $\mathbf{u}_t(\mathbf{x})$ and therefore $\mathbf{v}_t(\mathbf{x}; \theta)$ generates the desired probability path $p_t(\mathbf{x})$. Thus, we can train a CNF without access to the marginal vector field $\mathbf{u}_t(\mathbf{x})$ or probability path $p_t(\mathbf{x})$. Compared to the prior approaches to train flow models, Flow Matching allows simulation-free training with unbiased gradients, and scales easily to high dimensions.